Density Functional Studies of Oxidized and Reduced Methane Monooxygenase. Optimized Geometries and Exchange Coupling of Active Site Clusters

Timothy Lovell,* Jian Li,† and Louis Noodleman*

Department of Molecular Biology TPC-15, The Scripps Research Institute, La Jolla, California 92037

Received January 29, 2001

The conflicting protein crystallography data for the oxidized form ($MMOH_{ox}$) of methane monooxygenase present a dilemma regarding the identity of the solvent-derived bridging ligands within the active site: do they comprise a diiron unit bridged by $1H_2O$ and $1OH^-$ as postulated for *Methylococcus capsulatus* or $2OH^-$ ligands as suggested for *Methylosinus trichosporium*? Using models derived explicitly from the *M. capsulatus* and *M. trichosporium* protein data, spin-unrestricted density functional methods have been used to study two structurally characterized forms of the hydroxylase component of methane monooxygenase. The active site geometries of the oxidized ($MMOH_{ox}$) and two-electron-reduced ($MMOH_{red}$) states have been geometry optimized using several quantum cluster models which take into account the antiferromagnetic (AF) and ferromagnetic (F) coupling of electron spins. Trends in cluster geometries, energetics, and Heisenberg *J* values have been evaluated. For the majority of models, calculated geometries are in good agreement with the X-ray analyses and appear relatively insensitive to the F or AF alignment of electron spins on adjacent Fe sites. Discrepancies between calculation and experiment appear in the orientation of the coordinated His and Glu amino acid side chains for both $MMOH_{ox}$ and $MMOH_{red}$ and also in unexpected intramolecular proton transfer in the $MMOH_{ox}$ cluster models. There is additional dispersion between (and among) calculated and experimental $Fe^{3+}-OH^-$ distances with relevance to the correct protonation state of the solvent-derived ligands. In an accompanying paper (Lovell, T.; Li, J.; Noodleman, L. *Inorg. Chem.* **2001**, *40*, 5267), a comparison of the related energetics of the active site models examined herein is further evaluated in the full protein and solvent environment.

I. Introduction

Proteins that contain one or more transition metals as an important constituent of their active site (metalloproteins) are now known to play a crucial role in biology, particularly in processes involving coupled electron and proton transfer and where small molecules are chemically transformed.[1] Among the family of binuclear non-heme iron proteins,[2] hemerythrin, methane monooxygenase, ribonucleotide reductase, and stearoyl acyl carrier protein Δ^9-desaturase are well-known. All four proteins have attracted considerable interest during recent years, the majority of which has stemmed from the potential environmental, medical, and agricultural benefits that stand to be gained from a better understanding of the general principles governing their function and reactivity on the microscopic level. Several reviews[3] have thus appeared concerning different aspects of their molecular and electronic structures and biochemical functions.

Hemerythrin (Hr)[4] is a respiratory protein found in the four phyla of marine invertebrates. Its function is to bind, carry, and release molecular oxygen (O_2) without irreversible electron transfer or redox reaction leading to O−O bond cleavage and further oxidation chemistry. The hydroxylase component of methane monooxygenase (MMOH)[5] is found in anaerobic methanotrophic bacteria and catalyzes methane (CH_4) oxidation. The conversion of CH_4 into a more utilizable form has attracted a great deal of attention recently and is of obvious importance with respect to the regulation of the global concentration of this greenhouse gas. The R2 protein of ribonucleotide reductase (RNR)[6] plays a central role in the operation of all living organisms, providing cells with the precursors required for the first step in DNA synthesis[7] by catalyzing the reduction of ribonucleotides to their 2′-deoxyribonucleotide counterparts. This critical role in DNA replication has potential implications for intervention in the cycles of cancer cells and of viruses (herpes simplex) which encode RNR for their activity. Stearoyl acyl carrier protein desaturase (Δ^9D) is a plastid-localized non-membrane-bound soluble desaturase that appears in leafy green plants. Δ^9D functions to introduce the first double bond into saturated fatty acids, resulting in the corresponding mono-

* Authors to whom correspondence should be addressed. E-mail: tlovell@scripps.edu and lou@scripps.edu. Fax: +1 858 784 8896.

† Present address: Texas Biotechnology Corporation, 7000 Fannin Street, Houston, TX 77030.

(1) Holm, R. H.; Kennepohl, P.; Solomon, E. I. *Chem. Rev.* **1996**, *96*, 2239.

(2) Solomon, E. I.; Brunold, T. C.; Davis, M. I.; Kemsley, J. N.; Lee, S.-K.; Lehnert, N.; Neese, F.; Skulan, A. J.; Yang, Y.-S.; Zhou, J. *Chem. Rev.* **2000**, *100*, 235.

(3) (a) Feig, A.; Lippard, S. J. *Chem. Rev.* **1994**, *94*, 759. (b) Wallar, B. J.; Lipscomb, J. D. *Chem. Rev.* **1996**, *96*, 2625. (c) Andersson, K.; Gräslund, A. *Adv. Inorg. Chem.* **1995**, *43*, 359. (d) Stenkamp, R. E. *Chem. Rev.* **1994**, *94*, 715. (e) Lindqvist, Y.; Huang, W.; Schneider, G.; Shanklin, J. *EMBO J.* **1996**, *15*, 4081.

(4) (a) Klotz, I. M.; Kurtz, D. M., Jr. *Acc. Chem. Res.* **1984**, *17*, 1622. (b) Wilkins, P. C.; Wilkins, R. G. *Coord. Chem. Rev.* **1987**, *79*, 195.

(5) (a) Rosenzweig, A. C.; Nordlund, P.; Takahara, P. M.; Frederick, C. A.; Lippard, S. J. *Chem. Biol.* **1995**, *2*, 409. (b) Elango, N.; Radhakrishnan, R.; Froland, W. A.; Wallar, B. J.; Earhart, C. A.; Lipscomb, J. D. Olendorf, D. O. *Protein Sci.* **1997**, *6*, 556. (c) Rosenzweig, A. C.; Frederick, C. A.; Lippard, S. J.; Nordlund, P. *Nature* **1993**, *366*, 537.

(6) (a) Reichard, P. *Science* **1993**, *260*, 1773. (b) Stubbe, J.; van der Donk, W. A. *Chem. Rev.* **1998**, *98*, 705.

(7) (a) Stubbe, J *J. Biol. Chem.* **1990**, *265*, 5329. (b) Sjöberg, B.-M.; Gräslund, A. In *Advances in Inorganic Biochemistry*; Theil, E. C., Eichorn, G. L., Marzilli, L. G., Eds.; Elsevier: New York, 1983; Vol. 5, pp 87−110. (c) Reichard, P.; Ehrenberg, A. *Science* **1983**, *221*, 514.

10.1021/ic010115j CCC: $20.00
Published on Web 08/29/2001

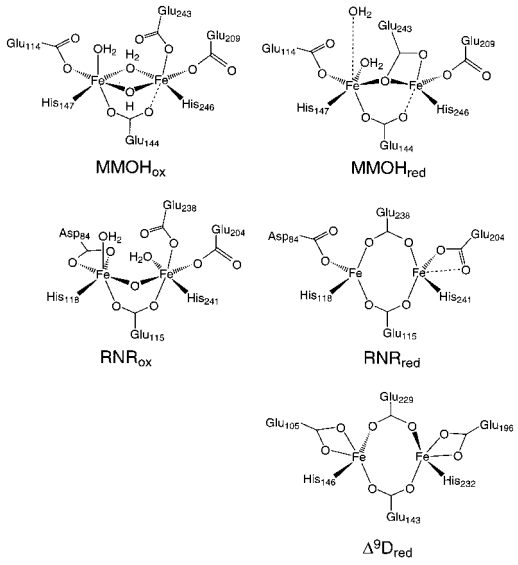

Figure 1. The structurally related diiron cores of the binuclear nonheme iron proteins. Methane monooxygenase: diferric MMOH$_{ox}$ (top left); diferrous MMOH$_{red}$ (top right). Ribonucleotide reductase: diferric RNR$_{ox}$ (middle left); diferrous RNR$_{red}$ (middle right). Stearoyl ACP desaturase: diferrous Δ^9D$_{red}$ (bottom right). Only the diferric core from *M. capsulatus* is shown.

unsaturated fatty acid.[8,9] The desaturases therefore play an important role in plant metabolism and have long been associated with the possible use of plant oils as renewable sources for reduced carbon.

Although there are no obvious similarities between the functionally distinct reactions carried out by these proteins, the important step in which the O−O bond is reduced and cleaved in order to prepare the active site for subsequent reaction chemistry is a feature of the enzymatic catalysis shared by MMO, RNR, and Δ^9D. Apart from minor differences in the orientation of coordinated protein side chains, this preparatory reaction occurs at metalloprotein active sites that are structurally similar (Figure 1). The similarity extends beyond the simple structures of the active sites and also includes the tertiary folds of the active domain of each protein, as well as a common proposed reaction mechanism, and in combination, all three factors suggest an evolutionary connection. Thus, rather than restrict our attention to one protein in particular, the distinct structural and mechanistic relationship between MMO, RNR, and Δ^9D suggests that an analysis of all three proteins may prove insightful. In this paper, the focus is on MMO, while the results of our calculations on RNR and Δ^9D will be reported in subsequent work.

Soluble MMO is an enzyme produced by methanotrophic bacteria,[10] which catalyzes the hydroxylation of methane to methanol and water by reaction with O_2 and NADH:

$$CH_4 + NADH + H^+ + O_2 \rightarrow CH_3OH + NAD^+ + H_2O$$

Methanotrophic bacteria are therefore capable of metabolizing one of the most inert hydrocarbons, CH_4, as their sole source of carbon and energy, allowing for rapid growth in vivo. Thus, anaerobic methanotrophic bacteria play an important environmental role in CH_4 consumption, by limiting its flow to the atmosphere and effectively regulating global concentrations of CH_4. Apart from their obvious biological and ecological importance, MMO is also known to oxidize a broad range of hydrocarbons,[11] leading to several other potential applications of the bacteria, but presently the mechanism by which MMO performs this unique conversion is unknown. However, a complete understanding of this process at the more fundamental molecular level may form a basis for the design of more efficient hydroxylation catalysts capable of utilizing the natural gases of the planet.

The soluble form of MMO is known for two methanotrophs, *Methylococcus capsulatas* (Bath), denoted as Mc from this point onward, and *Methylosinus trichosporium*, denoted as Mt, each of which consists of three component proteins: a hydroxylase,[5] denoted MMOH, of 245 kDa molecular weight and subunit composition $\alpha_2\beta_2\gamma_2$, and ultimately, the site of dioxygen activation and substrate conversion; a reductase, denoted MMOR, of 40 kDa including FAD and a 2Fe-2S cluster whose function is to transfer electrons from NADH to the hydroxylase; and a monomeric coupling protein called component B, represented as MMOB, of 16 kDa, that contains no metals or cofactors but which facilitates and regulates the rate of substrate oxidation by modulating electron transfer between the reductase and the hydroxylase.

Experimental studies have characterized the structure of the catalytic core of the MMOH component to reasonably high resolution for two oxidation states of the enzyme, denoted as the oxidized or resting state, MMOH$_{ox}$, and the two-electron-reduced state, MMOH$_{red}$, respectively. Spectroscopic (Mössbauer, XAS, EXAFS, ENDOR)[12] and magnetic resonance studies (EPR)[13] in conjunction with X-ray crystallographic analyses[5] of the resting state of the hydroxylase reveal two high-spin, antiferromagnetically (AF) coupled Fe(III) ions separated by ∼3.00−3.15 Å in an environment exclusively occupied by oxygen (Oϵ1 or Oϵ2) and nitrogen (Nδ1) donor atoms of glutamate (Glu) and histidine (His) protein residues. Within the first coordination shell, solvent-derived ligands such as H_2O and its deprotonated form, OH^-, complete the approximately octahedral coordination about each Fe(III) site. Apart from minor differences in the orientation of the protein side chains, these

(8) (a) Shanklin, J.; Somerville, C. *Proc. Natl. Acad. Sci. U.S.A* **1991**, *88*, 2510. (b) McKeon, T. A.; Stumpf, P. K. *J. Biol. Chem.* **1982**, *257*, 12141.

(9) (a) Nagai, J.; Bloch, K. *J. Biol. Chem.* **1968**, *243*, 4626. (b) Holloway, P. W. In *The Enzymes*, 3rd ed.; Boyer, P. D., Ed.; Academic: New York, 1983; pp 63−83. (c) Schmidt, H.; Heinz, E. *Plant Physiol.* **1990**, *94*, 214.

(10) (a) Liu, K. E.; Lippard, S. J. *Adv. Inorg. Chem.* **1995**, *42*, 263. (b) Dalton, H. *Adv. Appl. Microbiol* **1980**, *26*, 71. (c) Anthony, C. *The Biochemistry of Methanotrophs*; Academic: London, 1982.

(11) (a) Colby, J.; Stirling, D. I.; Dalton, H. *Biochem. J.* **1977**, *165*, 395. (b) Fox, B. G.; Borneman, J. G.; Wackett, L. P.; Lipscomb, J. D. *Biochemistry* **1990**, *29*, 6419. (c) Green, J.; Dalton, H. *J. Biol. Chem.*, **1989**, *264*, 17698.

(12) (a) Derose, V. J.; Liu, K. E.; Kurtz, D. M., Jr.; Hoffman, B. M.; Lippard, S. J. *J. Am. Chem. Soc.* **1993**, *115*, 6440. (b) Thomann, H.; Bernardo, M.; McCormick, J. M.; Pulver, S.; Andersson, K. K.; Lipscomb, J. D.; Solomon, E. I. *J. Am. Chem. Soc.* **1993**, *115*, 8881. (c) Fox, B. G.; Froland, W. A.; Dege, J. E.; Lipscomb, J. D. *J. Biol. Chem.* **1989**, *264*, 10023. (d) Fox B. G.; Hendrich, M. P.; Surerus, K. K.; Andersson, K. K.; Froland, W. A.; Lipscomb, J. D.; Münck, E. *J. Am. Chem. Soc.* **1993**, *115*, 3688. (e) Kauffmann, K. E.; Popescu, C. V.; Dong, Y. H.; Lipscomb, J. D.; Que, L., Jr.; Münck, E. *J. Am. Chem. Soc.* **1998**, *120*, 8739. (f) Ericson, A.; Hedman, B.; Hodgson, K. O.; Green, J.; Dalton, H.; Bentsen, J. G.; Beer, R. H.; Lippard, S. J. *J. Am. Chem. Soc.* **1988**, *110*, 2330. (g) Dewitt, J. G.; Rosenzweig, A. C.; Salifoglou, A.; Hedman, B.; Lippard, S. J.; Hodgson, K. O. *Inorg. Chem.* **1995**, *34*, 2505. (h) Shu, L. J.; Liu, Y.; Lipscomb, J. D.; Que, L., Jr. *J. Biol. Inorg. Chem.* **1996**, *1*, 297.

(13) (a) Woodland, M. P.; Patil, D. S.; Cammack, R.; Dalton, H. *Biochim. Biophys. Acta* **1986**, *873*, 237. (b) DeWitt, J. G.; Bentsen, J. G.; Rosenzweig, A. C.; Hedman, B.; Green, J.; Pilkington, S.; Papaefthymiou, G. C.; Dalton, H.; Hodgson, K. O.; Lippard, S. J. *J. Am. Chem. Soc.* **1991**, *113*, 9219. (c) Fox, B. G.; Surerus, K. K.; Münck, E. Lipscomb, J. D. *J. Biol. Chem.* **1988**, *263*, 10553.

findings are consistent for the most part for Mc and Mt within the first and second coordination spheres.

The oxidation of CH_4 occurs in a catalytic cycle where, in the first step, the diferric cluster, $MMOH_{ox}$, is reduced to the diferrous state, $MMOH_{red}$, by proton-coupled two-electron addition from NADH transferred by the iron−sulfur flavoprotein (MMOR). Analysis of the chemically reduced form of the enzyme by several techniques (XAS, EXAFS, MCD, EPR)[13,14] reveals two high-spin, very weakly ferromagnetically (F) coupled Fe(II) ions separated by ∼3.3 Å. EXAFS and MCD data indicate that the two Fe(II) atoms are 5-coordinate, suggesting significant structural rearrangement within the active site. This molecular reorganization is attributed to a carboxylate shift from terminal to μ1,1- or semi-bridging mode (via a single Oϵ2 atom of Glu243), with a water changing its coordination mode from bridging to terminal and a change in sign of the associated exchange coupling constant (*J*). The six protein side chain ligands remain coordinated, but the net loss of one water molecule coordinated to Fe, a shift in binding mode of a second water molecule from bridging to terminal Fe coordination, and a change in binding of a third water molecule from strong coordination to weak second-shell association renders each Fe(II) atom 5-coordinate and opens vacant nonadjacent coordination sites for further reaction chemistry.

In the next step of the cycle, docking of component B with MMOH results in structural rearrangement of the $MMOH_{red}$ site to an unknown form. The structurally undefined $MMOH_{red}$ subsequently binds and reacts with molecular O_2 to form first a metastable complex, denoted intermediate **O**, which very rapidly converts to a diferric−peroxo species, denoted intermediate **P**,[15] probably accompanied by another carboxylate shift which provides further open sites for O−O binding. Intermediate **P** is proposed to spontaneously rearrange to a diferryl−di-μ-oxo intermediate or related di-μ-oxo species, denoted intermediate **Q**,[15] which is the key catalytic intermediate capable of oxidizing methane to methanol. After the reaction of methane with intermediate **Q** and product release, the enzyme returns through proposed intermediates, **R** and **T**,[3b] to its native form, $MMOH_{ox}$. Despite the collective experimental effort, structures for **P**, **Q**, **R**, and **T** are not yet available, and as a result, many questions regarding the possible mechanism(s) of catalysis still remain unanswered. As more experimental data become available concerning the structures of the intermediates, attention naturally turns toward understanding not only the operation of the catalytically active species in isolation, but also in the presence of the full protein and solvent environment, and how the combined features affect the interconversion of one intermediate into another during enzyme turnover.

Modern quantum chemical methods are now being employed for detailed theoretical calculations of the electronic structures of metalloprotein active sites having relevance to biology.[16] Recent advances in the field, particularly in the density functional approach,[17,18] have permitted quantitative and qualitative analysis of the active sites of a number of metalloproteins.[19,20] Previous quantum mechanics based studies of MMO at various levels of theory have been employed to model aspects of the catalytic pathway.[21] Each successive study has provided significant insight into this complex system, with the majority focused toward identifying the structures and related energetics associated with the presently unknown key intermediates, **P** and **Q**.

However, the well-characterized X-ray structures of $MMOH_{ox}$ and $MMOH_{red}$ also raise a number of interesting questions for which fundamental issues still remain open. (1) Does the bridging coordination involve 2 OH^- groups or 1 H_2O and 1 OH^- ligand? (2) What are the relative energies of these structural possibilities with and without the presence of the exogenous acetate derived from the buffer in Mc? (3) Given the correct relative energies of the states $MMOH_{ox}$ and $MMOH_{red}$, by what mechanism do these two forms interconvert? (4) What is the role that the protein and solvent environment plays in the relative energetics in the early stages of the catalytic cycle? A deep understanding of such issues is complicated by the bonding of high oxidation state Fe to various solvent-derived and amino acid side chain based ligands during MMO turnover. Strong bonds are formed between the formally Fe(II) and Fe(III) ions and the OH^- ligands, while weaker bonds may be formed between the μ-carboxylato and H_2O ligands, especially those that reside in the second shell. At the same time, individual Fe sites retain a high-spin configuration and there is significant spin coupling, either F or AF between adjacent Fe sites via the oxygen-based and the μ1,3-carboxylato bridging ligands. A full understanding will clearly require a concerted view utilizing many different techniques. Thus, rather than attempt to delineate a complete picture of the methane to methanol conversion, as a starting point, spin-polarized density functional and electrostatics methods have been used to probe basic geometric and energetic issues associated with the $MMOH_{ox}$ and $MMOH_{red}$ forms of MMO.

(14) (a) Hendrich, M. P.; Munck, E.; Fox, B. G.; Lipscomb, J. D. *J. Am. Chem. Soc.* **1990**, *112*, 5861. (b) Pulver, S.; Froland, W. A.; Fox, B. G.; Lipscomb, J. D.; Solomon, E. I. *J. Am. Chem. Soc.* **1993**, *115*, 12409.

(15) (a) Liu, K. E.; Wang, D.; Huynh, B. H.; Edmondson, D. E.; Salifoglou, A.; Lippard, S. J. *J. Am. Chem. Soc.* **1994**, *116*, 7465. (b) Liu, K. E.; Valentine, A. M.; Wang, D.; Huynh, B. H.; Edmondson, D. E.; Salifoglou, A.; Lippard, S. J. *J. Am. Chem. Soc.* **1995**, *117*, 10174. (c) Liu, K. E.; Valentine, A. M.; Qiu, D.; Edmondson, D. E.; Appleman, E. H.; Spiro, T. G.; Lippard, S. J. *J. Am. Chem. Soc.* **1995**, *117*, 4997. (d) Lee, S.-K.; Lipscomb, J. D. *Biochemistry* **1999**, *38*, 4423. (e) Valentine, A. M.; Stahl, S. S.; Lippard, S. J. *J. Am. Chem. Soc.* **1999**, *121*, 3876. (f) Shu, L.; Nesheim, J. C.; Kauffmann, K.; Münck, E.; Lipscomb, J. D.; Que, L., Jr. *Science* **1997**, *117*, 515.

(16) Siegbahn, P. E. M.; Blomberg, M. R. A. *Chem. Rev.* **2000**, *100*, 439.

(17) (a) Ziegler, T. *Chem. Rev.* **1991**, *91*, 651. (b) Ziegler, T. *Can. J. Chem.* **1995**, *73*, 743.

(18) Versluis, L.; Ziegler, T. *J. Chem. Phys.* **1988**, *88*, 322.

(19) Noodleman, L. *J. Chem. Phys.* **1981**, *74*, 5737.

(20) (a) Bencini, A.; Gatteschi, D. *J. Am. Chem. Soc.* **1986**, *108*, 5763. (b) Aizman, A.; Case, D. A. *J. Am. Chem. Soc.* **1982**, *104*, 3269. (c) Ross, P. K.; Solomon, E. I. *J. Am. Chem. Soc.* **1991**, *113*, 3246. (d) Noodleman, L.; Case, D. A. *Adv. Inorg. Chem.* **1992**, *38*, 423. (e) Mouesca, J.-M.; Chen, J. L.; Noodleman, L.; Bashford, D.; Case, D. A. *J. Am. Chem. Soc.* **1994**, *116*, 11898. (f) Brunold, T. C.; Solomon, E. I. *J. Am. Chem. Soc.* **1999**, *121*, 8277. (g) Brunold, T. C.; Solomon, E. I. *J. Am. Chem. Soc.* **1999**, *121*, 8288. (h) Lovell, T.; McGrady, J. E.; Stranger, R.; Macgregor, S. A. *Inorg. Chem.* **1996**, *35*, 3079. (i) McGrady, J. E.; Lovell, T.; Stranger, R. *Inorg. Chem.* **1997**, *36*, 3242. (j) McGrady, J. E. *Angew. Chem., Int. Ed.* **2000**, *17*, 3077. (k) McGrady, J. E.; Lovell, T.; Stranger, R. *J. Phys. Chem. A* **1997**, *101*, 6265.

(21) (a) Yoshizawa, K.; Shiota, Y.; Yamabe, T. *Chem. Eur. J.* **1997**, *3*, 1160. (b) Yoshizawa, K.; Ohta, T.; Yamabe, T. *Bull. Chem. Soc. Jpn.* **1998**, *71*, 1899. (c) Yoshizawa, K. Ohta, T.; Yamabe, T.; Hoffman, R. *J. Am. Chem. Soc.* **1997**, *119*, 12311. (d) Yoshizawa, K.; Shiota, Y.; Yamabe, T. *J. Am. Chem. Soc.* **1998**, *120*, 564. (e) Yoshizawa, K.; Shiota, Y.; Yamabe, T. *Organometallics* **1998**, *17*, 2825. (f) Yoshizawa, K. *J. Biol. Inorg. Chem.* **1998**, *3*, 318. (g) Yoshizawa, K.; Yamabe, T.; Hoffman, R. *New J. Chem.* **1997**, *21*, 151. (h) Yoshizawa, K.; Hoffman, R. *Inorg. Chem.* **1996**, *35*, 2409. (i) Siegbahn, P. E. M.; Crabtree, R. H. *J. Am. Chem. Soc.* **1997**, *119*, 3103. (j) Siegbahn, P. E. M. *Inorg. Chem.* **1999**, *38*, 2880. (k) Siegbahn, P. E. M.; Crabtree, R. H.; Nordlund, P. *JBIC, J. Biol. Inorg. Chem. Soc.* **1998**, *3*, 314. (l) Basch, H.; Mogi, K.; Musaev, D. G.; Morokuma, K. *J. Am. Chem. Soc.* **1999**, *121*, 7249. (m) Dunietz, B. D.; Beachy, M. D.; Cao, Y.; Whittington, D. A.; Lippard, S. J.; Friesner, R. A. *J. Am. Chem. Soc.* **2000**, *122*, 2828. (n) Torrent, M.; Musaev, D. G.; Morokuma, K. *J. Phys. Chem. B* **2001**, *105*, 4453.

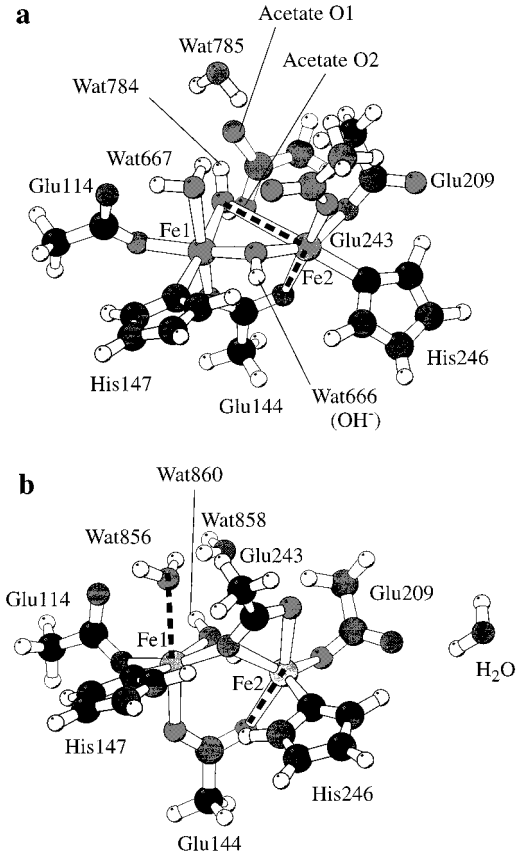

Figure 2. (a) The active site structure of $MMOH_{ox}$ from *M. capsulatus* including the exogenous acetate. (b) The active site structure of $MMOH_{red}$. The structures were prepared using MOLSCRIPT: Kraulis, P. J. *J. Appl. Crystallogr.* **1991**, *24*, 946.

II. Quantum Active Site Models

The different combinations of ligands used in our quantum cluster models to represent the active sites are depicted in Figure 2a for $MMOH_{ox}$ and Figure 2b for $MMOH_{red}$, and are summarized in Table 1 along with the relevant charge on each cluster. Weak coordination to an Fe site based on the X-ray analyses of the Mc protein is indicated by the bold dashed line in Figure 2a and Figure 2b. For the resting form in Figure 2a, the six protein side chain ligands bound to the iron sites derive from two histidine residues, His147 and His246, and four glutamic acid residues, Glu114, Glu144, Glu209, and Glu243. Approximately octahedral coordination about each iron site is completed by the addition of a solvent water (Wat667) molecule bound terminally to one of the iron sites (Fe1), a bridging OH^- (Wat666), and a bridging H_2O molecule (Wat784). This depicts our model A and B clusters (Table 1). Models A and B are identical except for the constraints imposed upon the O−H distance of the bridging OH^- (Wat666) ligand. In model A, the O-H group is unconstrained and has all degrees of freedom available. In model B, the O-H distance is fixed to that of a standard O−H bond so that there can be no net internal proton transfer.[22a] Overall the active site is a charged cluster which can form strong hydrogen bonds to the surrounding protein residues and nearby solvent ligands. Table 2 summarizes important hydrogen-bonding interactions between first- and second-shell ligands in the protein after optimization of the hydrogen-bonding network. Important hydrogen bonds are described in more detail in an accompanying paper (referred to from this point onward as P2)[22b] whereby a more complete analysis of the protein field electrostatics is examined.

Within the first ligand shell, the Glu209.Oϵ1 atom not coordinated to Fe2 accepts a hydrogen bond from Gln140. Nϵ2-Hϵ2 that resides in the second ligand sphere (see Table 2). Here, the Glu209.Oϵ1···Nϵ2.Gln140 distance of 3.28 Å falls outside the standard or typical range[23] of (2.9 ± 0.1) Å of accepted hydrogen-bonding distances between amide-type and carbonyl-type ligands and the resulting hydrogen bond distance of 2.54 Å is rather long. Coupled with size of the Glu209.Oϵ1···Hϵ2.Nϵ2.Gln140 angle (128.3°), it further suggests that this hydrogen bond should be relatively weak. Since no other hydrogen-bonding partner is within 3.0 Å of Glu209.Oϵ1, this weak hydrogen bond is assumed sufficient to saturate the coordination vacancy of the open Glu209.Oϵ1 atom. The hydrogen-bonding partners appropriate to His246, His147, and Glu114 are also shown in Table 2. Glu243.Oϵ1 was not observed to coordinate to the Fe sites nor to any of the other first/second-shell protein residues, but was assumed previously on the basis of the structural data to be coordinatively saturated from a hydrogen bond to Wat667 bound terminally to Fe1.[5a] This possibility cannot be discounted, but it is also worth noting that the active site cavity of protomer A of Mc (and of Mt) also contains a third water molecule, denoted Wat785, whose position favors stronger hydrogen bonding to Glu243.Oϵ1 (Figure 2a). Model B is then augmented by addition of a second-shell Wat785 molecule that lies within hydrogen-bonding distance (Glu243.Oϵ1···O.Wat785 = 2.76 Å) of Glu243.Oϵ1. The resulting cluster is denoted as model C. Although Wat785 is hydrogen bonded neither to Thr213 nor to Wat667, it is also worth noting that it lies on the pathway between them and potentially links Thr213 to the active site. The X-ray structure of Mt suggests that the two bridging ligands may be OH^- molecules, denoted Wat1 and Wat2 in the 1MHY X-ray structure:[5b] to construct this cluster, the bridging Wat784 in models A and B was replaced by an OH^- ligand to produce cluster model D (Table 1). In Mc,[5a] the low-temperature X-ray structure of the catalytic center was crystallized with an exogenous acetate (from the NH_4OAc buffer) in the second coordination shell, while for Mt,[5b] the acetate was absent (and observed to be replaced by a cluster of several water molecules). The acetate lies within hydrogen-bonding distance ($Ac.O_1$···O.Wat784 = 2.62 Å, $Ac.O_2$···O.Wat784 = 2.97 Å) of the bridging Wat784 molecule and thus may be associated with the bridging water ligand. The geometric influences from addition of the second-shell acetate on the nature of the bridging ligands are incorporated into our model E (H_2O/OH^- bridge) and model F (2 OH^- bridge) clusters, respectively. The energetic consequences of the acetate are explored in the accompanying manuscript P2.[22b]

Upon two-electron reduction and addition of one proton to model B, or addition of two electrons plus two protons to model D, significant structural rearrangement within the active site occurs, and this is shown in Figure 2b. His147, His246, Glu114, Glu144, Glu209, Glu243, and Wat784 (it is worth noting that, for the Mc protein, the identification numbers used to distinguish solvent ligands are different in the two characterized forms and Wat784 in $MMOH_{ox}$ corresponds to Wat860 in $MMOH_{red}$) still remain coordinated to the Fe sites, while Wat856 (analogous to Wat667 in $MMOH_{ox}$), which is bound terminally to Fe1, is

(22) (a) The constraint of the O55−H56 bond to that of a standard O−H bond length was only applied to model B. In all other geometry optimizations, this parameter was allowed to vary. (b) Lovell, T.; Li, J.; Noodleman, L. *Inorg. Chem.* **2001**, *40*, 5267.

(23) Schulz, G. E.; Schrimmer, R. H. In *Principles of Protein Structure*; Cantor, C. R., Ed.; Springer-Verlag: New York, 1990; p 35.

Table 1. $MMOH_{ox}$ and $MMOH_{red}$ Active Site Cluster Models

model	core	+terminal ligands	+bridging	+variable	charge
			$MMOH_{ox}$		
A[a]	Fe_2	+Glu243 +Glu209 +Glu114 +His147 +His246 +Wat667	+Glu144	+Wat784 +Wat666(OH^-)	+1
B[b]				+Wat784 +Wat666(OH^-)	+1
C[c]				+Wat784 +Wat666(OH^-) +Wat785	+1
D[d]				+Wat784(OH^-) +Wat666(OH^-)	0
E[e]				+Wat784 +Wat666(OH^-) +acetate	0
F[f]				+Wat784(OH^-) +Wat666(OH^-) +acetate	−1
			$MMOH_{red}$		
A[g]	Fe_2	+Glu209 +Glu114 +His147 +His246 +Wat856	+Glu144 +Glu243 +Wat860		0
B[h]				H_2O	0
C[i]				+Wat858 + H_2O	0

[a] A: Unconstrained H_2O/OH^- cluster. [b] B: H_2O/OH^- cluster, bridging $[O-H]^-$ distance constrained. [c] C: H_2O/OH^- cluster, plus second-shell Wat785 to H-bond to Glu243.Oϵ1. [d] D: 2 OH^- cluster. [e] E: H_2O/OH^- cluster + acetate. [f] F: 2 OH^- cluster + acetate. [g] A: Active site model from protein X-ray data excluding Glu209.Oϵ1 solvent-derived H-bonding partner. [h] B: Extra H_2O assigned to H-bond and saturate Glu209.Oϵ1 based on ref 21m. [i] C: Additional second-shell Wat858 assigned to model B.

Table 2. Hydrogen-Bonding Analysis for Second-Shell Protein Residues and Solvent Ligands for $MMOH_{ox}$

		distance (Å)			
acceptor	donor	acceptor−donor (range[a])	acceptor···H	angle (deg) donor-H···acceptor	H-bond partner[b]
Glu209.Oϵ1	Gln140.Nϵ2-Hϵ2	3.28 (2.9 ± 0.1)	2.54	128.3	yes[P]
Glu144.Oϵ2	Gln140.Nϵ2-Hϵ2	2.96	1.99	112.6	yes[P]
Gln140.O	Glu144.N	2.78	1.79	151.2	yes[P]
Asp143.Oδ2	His246.Nϵ2-Hϵ2	2.81 (2.9 ± 0.1)	1.76	169.7	yes[P]
Asp143.O	His147.N	2.78	1.76	167.1	yes[P]
Asp242.Oδ2	His147.Nϵ2-Hϵ2	2.72	1.67	175.0	yes[P]
Asp242.O	His246.N	3.81	2.97	139.0	no[P]
Glu243.O	His246.N	2.93	2.16	130.2	yes[P]
Glu111.O	Glu114.N	3.25	2.66	115.9	no[P]
His147.O	Gln150.N	3.19	2.80	102.5	no[P]
Glu114.Oϵ2	Wat667-H	2.54 (2.8± 0.1)	1.50	168.3	yes[Q]
Glu243.Oϵ1	Wat785-H	2.76	1.75	172.0	yes[Q]
Glu243.Oϵ1	Wat667-H	3.04	2.95	127.0	no[Q]

[a] Range means "typical" H-bonding range from ref 23. [b] P: Proton positions minimized using molecular mechanics in InsightII/Discover[24] for Mc and Mt protein. The data shown are for chain D of Mc, with the data for chain A of Mt being very similar. Q: Proton positions optimized in quantum active site in ADF for model C.

Table 3. Hydrogen-Bonding Analysis for Second-Shell Protein Residues and Solvent Ligands for $MMOH_{red}$

		distance (Å)			
acceptor	donor	acceptor−donor	angle (deg) acceptor···H	donor-H···acceptor	H-bond partner[a]
Glu209.Oϵ1	Gln140.Nϵ2-Hϵ2	3.61	3.04	115.6	no[P]
Glu144.Oϵ2	Gln140.Nϵ2-Hϵ2	3.00	2.15	141.7	yes[P]
Gln140.O	Glu144.N	2.75	1.78	154.1	yes[P]
Asp143.Oδ2	His246.Nϵ2-Hϵ2	2.76	1.75	159.3	yes[P]
Asp143.O	His147.N	2.87	1.85	170.9	yes[P]
Asp242.Oδ2	His147.Nϵ2-Hϵ2	2.73	1.70	169.3	yes[P]
Asp242.O	His246.N	3.66	2.76	146.3	no[P]
Glu243.O	His246.N	3.19	2.54	121.0	yes[P]
Glu111.O	Glu114.N	3.10	2.58	110.5	no[P]
His147.O	Gln150.N	3.43	3.05	102.9	no[P]
Glu114.Oϵ2	Wat856-H	2.60	1.90	171.0	yes[Q]
Wat856	Wat858-H	3.25	2.36	154.9	yes[Q]
Wat858	Wat860-H	2.77	1.81	160.0	yes[Q]

[a] P: Proton positions minimized using molecular mechanics in InsightII/Discover[24] for Mc protein, chain ALF1. Q: Proton positions optimized in quantum active site in ADF for model C.

weakly associated and appears in the second coordination sphere. This is depicted in our $MMOH_{red}$ cluster model A (Table 1). The relevant second-shell hydrogen-bonding partners for the His and coordinatively unsaturated Glu residues are indicated in Table 3. An examination of the $MMOH_{red}$ protein indicated that the same hydrogen-bonding partners are observed as for $MMOH_{ox}$ for the His147, His246, and Glu114 residues. However, the hydrogen bond between Glu209.Oϵ1 and Gln140.Nϵ2 appeared to be even weaker than in $MMOH_{ox}$, with Glu209.Oϵ1···Nϵ2.Gln140 = 3.61 Å and Glu209.Oϵ1···Hϵ2.Nϵ2.Gln140 = 3.04 Å and clearly beyond the boundary of acceptable weak hydrogen-bonding distances. Analysis of $MMOH_{red}$ revealed no other hydrogen-bonding partners to the Glu209.Oϵ1 atom, suggesting that Glu209.Oϵ1 was coordinatively unsaturated in the protein. Subsequent reexamination of the electron density map of the reduced protein

has implicated a water molecule, previously unassigned, as hydrogen bonding to Glu209.Oϵ1.[21m] We therefore added an additional H_2O to provide the hydrogen-bonding partner to Glu209.Oϵ1, and this $MMOH_{red}$ active site is denoted as model B (Table 1 and Figure 2b). Spectroscopic and X-ray studies suggest that each ferrous ion is 5-coordinate. A sixth ligand, Wat856, remains in the second sphere and coordinates only very weakly to Fe1. The structural implications and energetic consequences of the weakly bound Wat856 in the active site are currently unresolved. Given a favorable orientation of the water dipole, the vacant sixth coordination site on Fe1 would be potentially attractive for Wat856 binding, resulting in an Fe1 coordination of 6 and not 5. The question therefore arises "why is Wat856 not strongly coordinated to Fe1 but instead remains weakly bound in the second ligand shell?" No amino acid side chain or main chain hydrogen-bonding partners to Wat856 exist, but several structurally characterized water molecules in the near vicinity, such as Wat858, may provide the necessary hydrogen-bonding network that supports Wat856 remaining only weakly associated with Fe1. To test this hypothesis, the structurally observed Wat858 is incorporated into our model C $MMOH_{red}$ calculation.

For all our active site cluster models, within the first coordination shell, histidine residues were approximated as neutral imidazole rings, while glutamate residues were replaced by charged acetate groups. The active site model is regarded as a small part of the protein, terminating with one H atom in place of the appropriate linking C atom. The Cβ atoms of the histidine and glutamate residues were therefore replaced by Hβ atoms to saturate the quantum clusters. These atoms lie at the interface of the quantum and classical regions and thus were treated in an appropriate manner to conserve charge. Starting geometries were taken explicitly from the crystal structure data[5] following optimization of the hydrogen-bonding network[24] while the final geometries were computed by the density functional methods described in the following section.

III. Computational Methodology

The computations in this paper are based on density functional theory;[17,25] an in-depth theoretical background and detailed discussion can be found elsewhere. The details of the DF calculations (the first step toward obtaining the energetics in the protein environment) and relevant parameters are discussed below. The Amsterdam Density functional package (ADF, version 2.3)[26] was employed to compute the geometries and energies of the active site clusters. The ADF basis set IV was used to model Fe atoms and basis set IV for the main group atoms C, N, O, and H, which correspond to uncontracted triple-ζ Slater-type orbitals (STO) for the 4s, 4p, and 3d valence orbitals of Fe, triple-ζ STOs for 2s, 2p valence orbitals of C, N, O augmented with a 3d polarization orbital, and triple-ζ STO for 1s of H with a 2p polarization orbital.[27] The inner core orbitals were treated by the frozen core approximation. An auxiliary charge density fit set that consists of s, p, d, f, and g STO functions accompanies the corresponding orbital basis sets IV and III, and was adopted to fit the molecular density and used to calculate the Coulomb and exchange potentials.[28] The numerical integration scheme was the polyhedron method developed by te Velde et al.[29] For all geometry optimizations, the analytical gradient method implemented by Versluis et al.[18] was used along with a numerical integration accuracy of 4.0. The optimizations used the Newton−Raphson method, and the Hessian was updated with the Broyden−Fletcher−Goldfard−Shanno scheme.[30] Convergence criteria were set to 0.001 Å in coordinates and 0.01 Hartree/Å in the norm of all gradient vectors. For charged and spin-polarized complexes (such as diiron active sites), the geometry optimizations in this paper were done at the GGA level (Vosko−Wilk−Nusair (VWN) parametrization for the LDA)[31] with the generalized gradient correction terms included in the SCF as introduced by Perdew and Wang (PW91)[32] to the exchange and correlation.

To deal with the spin polarization and spin coupling in the diiron clusters, all density functional calculations were done with the spin-unrestricted method. The broken-symmetry (BS) approach[19] was adopted to tackle the antiferromagnetic coupling between the Fe sites. The BS state is not a pure spin state; rather it is a mixture of pure spin states, in which the majority spin and minority spin electrons on a specific atomic site are arranged either spin up and spin down or the converse to give a spin-coupling pattern with the correct net total spin and either an overall antiferromagnetic or ferromagnetic alignment. The energy of such a BS state is usually above, but close to, the true ground state energy. A spin projection scheme can be used to obtain the true ground state energy, but in the majority of cases, spin projection reveals that the broken-symmetry state lies close to the true ground state.[20k] To construct a desired BS state, a calculation on the high-spin (HS) state was first completed, which is a pure spin state described by a single determinant, with all unpaired electrons aligned in the same direction (spin up) to adopt the highest possible total spin state S of 5 ($2Fe^{3+}$) or 4 ($2Fe^{2+}$). The SCF converged fit density of the HS state was then manipulated by exchanging designated blocks of α and β electron densities. In this way, the starting density for the required spin-flipped state was created, from which BS states were obtained.

The active sites of the non-heme iron proteins are relatively large: 56 atoms (models A and B), 59 (model C), 55 (model D), 63 (model A/B + acetate = model E), and 62 (model D + acetate = model F) for $MMOH_{ox}$, and 54 (model A), 57 (model B), and 60 (model C) for $MMOH_{red}$. All calculations were performed on either SGI Power Challenge (12CPU, R10000 chip, 195 MHz) or SGI Origin series (16CPU, R10000 chip, 250 MHz) workstations at The Scripps Research Institute. Timing statistics are given in the Supporting Information. Calculations were done without symmetry (NoSym) using the parallelized version of the ADF code on four nodes for optimal scaling efficiency. For geometry optimizations, within the first ligand sphere, water or hydroxide molecules were allowed all degrees of freedom. All bond lengths and angles associated with atoms ligated to the Fe centers derived from amino acid residues were optimized. The remaining internal geometries of coordinated protein residues within the first shell were constrained to the experimental values. This approach was applied for two reasons: (1) to maintain reasonable fidelity with the experimental structures and thus represent the effects of second-

(24) (a) *Insight II Users Guide*; Biosym Technologies: San Diego, CA, 1995. (b) Brooks, B. R.; Bruccoleri, R. E.; Olafson, B. D.; States, D. J.; Swaminathan, S.; Karplus, M. *J. Comput. Chem.* **1983**, *4*, 187. (c) Heavy-atom coordinates were extracted from the X-ray data. H atom positions were optimized using standard InsightII (Discover module, BioSym/MSI) minimization procedures, using formal metal charges (3+/2+) assigned to the Fe sites, while the total charge for each single amino acid residue was assigned the appropriate integer charge (+1, 0, or −1) as a sum of the partial atom charges obtained from the standard InsightII amino acid fragment libraries. During the hydrogen atom optimization for the active domain of the protein, all heavy-atom positions were kept fixed.

(25) (a) *Density functional methods in chemistry*; Labanowski, J. K., Andzelm, J. W., Eds.; Springer-Verlag: New York, 1991. (b) Deeth, R. J. *Struct. Bonding* **1995**, *82*, 1.

(26) *ADF 2.3.0*; Department of Theoretical Chemistry, Free University of Amsterdam: Amsterdam, The Netherlands, 1997.

(27) (a) Snijders, J. G.; Baerends, E. J.; Vernooijs, P. *At. Nucl. Data Tables* **1982**, *26*, 483. (b) Vernooijs, P.; Snijders, J. G.; Baerends, E. J. *Slater Type Basis Functions for the Whole Periodic System*; internal report; Free University of Amsterdam: Amsterdam, The Netherlands, 1981.

(28) Krijn, J.; Baerends, E. J. *Fit Functions in the HFS-method*; internal report (in Dutch): Free University of Amsterdam: Amsterdam, The Netherlands, 1984.

(29) (a) Boerrigter, P. M.; te Velde, G.; Baerends, E. J. *Int. J. Quantum Chem.* **1988**, *33*, 87. (b) te Velde, G.; Baerends, E. J. *J. Comput. Phys.* **1992**, *99*, 84.

(30) Schlegel, H. B. In *Ab initio Methods in Quantum Chemistry—I*; Lawley, K. P., Ed.; Adv. Chem. Phys. 67; Wiley: New York, 1987.

(31) Vosko, S. H.; Wilk, L.; Nusair, M. *Can. J. Phys.* **1980**, *58*, 1200.

(32) Perdew, J. P.; Chekavry, J. A.; Vosko, S. H.; Jackson, K. A.; Perderson, M. R.; Singh, D. J.; Fioihais, C.*Phys. Rev. B* **1992**, *46*, 6671.

Table 4. Calculated and Experimental Interatomic Distances (Å) for $MMOH_{ox}$

			active site model							Mc			
atom	atom	ligand type	A[a,h]	B[b,h]	C(tI)[c]	C(tII)	D[d,h]	E-f (E-p)[e,h]	F-f (F-p)[f,h]	prot A[g]	prot B[g]	av	Mt
Fe1	Fe2		3.13	3.19	3.34	3.17	3.11	3.33 (3.18)	3.01 (3.11)	3.04	3.14	3.09	2.99
Fe1	O45	O_t	1.97	1.97	1.97	1.97	2.01	2.03 (1.97)	2.12 (2.01)	1.91	1.96	1.94	1.89
Fe1	N36	N_t	2.15	2.15	2.13	2.14	2.19	2.19 (2.15)	2.23 (2.19)	2.00	2.19	2.10	2.23
Fe1	O3	μCO_2	1.98	1.97	2.09	2.00	2.00	2.11 (1.97)	1.95 (2.00)	2.00	2.19	2.10	2.05
Fe1	O55	μOH	1.80	1.86	1.93	1.82	2.01	1.85 (1.85)	2.21 (2.20)	1.78	1.62	1.70	1.71
Fe1	O10	O_t	2.24	2.17	2.15	2.23	2.22	2.25 (2.17)	2.20 (2.22)	2.28	2.27	2.28	2.23
Fe1	O52	μH_2O	2.25	2.26	2.27	2.29	2.01	1.92 (2.03)	1.86 (1.87)	2.43	2.24	2.34	2.15
Fe2	O20	O_t	1.96	1.95	1.93	1.94	2.01	1.91 (1.95)	2.09 (2.01)	1.96	1.85	1.91	2.01
Fe2	N27	N_t	2.07	2.06	2.06	2.06	2.11	2.09 (2.06)	2.16 (2.11)	2.32	2.08	2.20	2.26
Fe2	O13	O_t	2.09	1.93	1.93	2.08	2.00	1.96 (1.93)	2.00 (2.00)	1.95	2.04	2.00	1.86
Fe2	O4	μCO_2	2.44	2.43	2.44	2.44	2.44	2.43 (2.43)	2.43 (2.44)	2.44	2.56	2.50	2.29
Fe2	O55	μOH	1.77	1.78	1.88	1.79	1.98	1.90 (1.78)	2.06 (1.98)	1.94	2.02	1.98	2.04
Fe2	O52	μH_2O	3.24	3.28	3.41	3.28	2.16	3.26 (3.19)	1.89 (1.99)	2.58	2.51	2.55	2.17
O10	O47		2.54	2.55	2.50	2.51	2.54	2.54 (2.54)	2.58 (2.54)	2.92	2.65	2.79	2.66
O10	O15		2.93	2.89	3.05	2.99	3.02	3.03 (2.88)	2.97 (3.02)	2.74	3.16	2.95	2.80
O10	O55		2.73	2.72	2.77	2.74	2.74	2.83 (2.72)	3.20 (3.04)	2.58	2.76	2.67	2.74
O55	H56		1.95	1.00	1.04	1.91	1.05	1.00 (1.00)	1.04 (1.04)				
H56	O15		1.00	1.74	1.64	1.01	1.59	1.76 (1.72)	1.90 (1.90)				
O52	H53		1.00	1.00	1.00	1.00	0.95	1.53 (1.00)	1.44 (1.27)				
H53	O58							1.03 (2.06)	1.06 (1.15)				

[a] A: Unconstrained H_2O/OH^- cluster. [b] B: H_2O/OH^- cluster, O55−H56 distance constrained.[22a] [c] C: H_2O/OH^- cluster, plus Wat785 to H-bond to Glu243.Oϵ1. [d] D: 2 OH^- cluster. [e] E-f: Model B cluster + $CH_3CO_2^-$(full opt.). E-p: Model B cluster + $CH_3CO_2^-$(partial opt.). [f] F-f: Model D cluster + $CH_3CO_2^-$(full opt.). F-p: Model D cluster + $CH_3CO_2^-$(partial opt.). [g] Protomers A and B are the two crystallographically independent halves of the $\alpha_2\beta_2\gamma_2$ hydroxylase dimer of Mc, for which standard deviations in the experimental bond lengths are ~0.20 Å, ref 5a. [h] Note: Model D has one atom less than model A or B, and model F has one atom less than model E. For clarity with Table 6, the atom numbers of model A or B and model E are adopted.

shell protein and solvent hydrogen-bonding effects without the need to expand to overly large quantum clusters and (2) to avoid continual rotation (free-rotor-like motion) about the metal−ligand bonds and thus ensure that the orientation of both the histidine rings and glutamate residues was such that the position of the linking Cβ atoms at the quantum/protein interface was preserved in an approximate way, prior to docking the optimized active cluster back into the protein environment. To take account of the problems associated with SCF convergence (due to the small HOMO−LUMO gaps of ~0.01 eV or less) when starting from the X-ray coordinates, SCF convergence was achieved by artificially shifting the virtual orbitals to higher energy. The converged wave function and geometry were then used as the starting point for our geometry optimization calculations where artificially shifting the virtual orbitals to higher energy was not required.

Spectroscopic analysis of $MMOH_{ox}$ and $MMOH_{red}$ indicates that the Fe atoms are all high spin. $MMOH_{ox}$ displays weak antiferromagnetic exchange coupling to an overall ground state of $S = 0$ that is diamagnetic, while $MMOH_{red}$ is best described by ferromagnetic coupling of two $S = 2$ single ions to give an $S = 4$ ground state. In density functional theory, exchange coupling constants (J) in dinuclear transition metal complexes can be evaluated using spin-projection methods from the energy difference between a high-spin state and a broken-symmetry state.[20b,e] Typically, spin coupling in transition metal dimers is evaluated by determining the Heisenberg coupling parameter in the spin Hamiltonian, most commonly defined in the non-heme diiron protein literature as

$$H = -2J\vec{S}_1\cdot\vec{S}_2 \qquad (1)$$

where S_1 and S_2 are the site spin vectors on the adjacent subunits, formally associated with the ferric (S_1, $S_2 = {}^5/_2$) or ferrous (S_1, $S_2 = {}^4/_2$) ions. The J coupling constant determines the entire ladder of spin states of the spin-coupled system, with relative energies given by

$$E(S) = -JS(S+1) \qquad (2)$$

Importantly, the broken-symmetry state is not a pure spin state but rather a weighted average of pure ($M_S = 0$) spin states. Since the weighting factor of each pure spin state is known, the energy difference can be expressed as a multiple of the J parameters. From Clebsch−Gordan algebra, this gives an expression for the broken-symmetry energy in terms of pure spin state energies,

$$E(S_{max} = S_1 + S_2) - E_{BS}(M_S = S_1 - S_2) = -4JS_1S_2 \qquad (3)$$

where, for diferric systems, $S_{max} = 5$, $M_S = 0$, and for diferrous systems, $S_{max} = 4$, $M_S = 0$. Thus, for isovalent systems, by formulating eq 3 in terms of HS and BS spin states and known spin quantum numbers, J can be extracted from the calculated energy difference from the left-hand side of eq 3.

IV. Results and Discussion

1. Geometry Optimization of Native Cluster Models for $MMOH_{ox}$ and $MMOH_{red}$. i. $MMOH_{ox}$. We begin with a comparison of our calculated geometries with the known experimental data. The high-resolution protein X-ray crystallographic data for Mc or Mt can be used to construct the coordination geometry of the diiron active site cluster. However, active site cluster models built up in this way are not accurate enough for quantum mechanical energy calculations due to uncertainties in metal−ligand bond lengths, angles, and torsions. The geometries of $MMOH_{ox}$ and $MMOH_{red}$ have been optimized using the geometry of the active site in the Mc protein as the starting point. Calculated interatomic distances are given in Table 4 for our $MMOH_{ox}$ model clusters with antiferromagnetic coupling, along with the accompanying X-ray structural data for the two characterized proteins. To gauge an overall picture of the reliability of the calculated geometries, they are RMSD matched using the Xfit[33] package of McRee et al. against those of the active sites from the Mc and Mt X-ray structures both with and without the hydrogen atoms included in the fitting algorithm. RMSD data are presented in Table 5 for the geometries arising from different spin alignments of electrons at the Fe sites, ferromagnetic ($MMOH_{ox}$, $S_{max} = 5$, $MMOH_{red}$, $S_{max} = 4$), referred to as high spin (HS), and antiferromagnetic (spin-flipped, $M_S = 0$), denoted as broken symmetry (BS), in each case.

(33) McRee, D. E.; Israel, M. In *Crystallographic Computing*; Bourne, E., Watenpaugh, K., Eds.; Oxford University Press: Oxford, 1998; Vol. 7.

Table 5. RMSD Values (Å) for Docked Optimized Cluster Models of $MMOH_{ox}$ and $MMOH_{red}$ to the Active Site in the Protein[a]

$MMOH_{ox}$

	docked to Mc				docked to Mt			
	all atoms		heavy atoms		all atoms		heavy atoms	
	$S_{max} = 5$	$M_S = 0$	$S_{max} = 5$	$M_S = 0$	$S_{max} = 5$	$M_S = 0$	$S_{max} = 5$	$M_S = 0$
A	1.03	1.03	0.75	0.75	0.96	0.96	0.74	0.74
B	1.01	1.01	0.75	0.75	0.96	0.96	0.74	0.74
C(tI)	1.00	1.00	0.75	0.75	0.96	0.96	0.75	0.75
C(tII)	1.00	1.00	0.74	0.74	0.96	0.96	0.75	0.75
D	0.89	0.89	0.75	0.75	0.90	0.90	0.68	0.68
E-p	1.34	1.34	1.12	1.12				
F-p	1.15	1.15	0.95	0.95				
E-f	1.04	1.04	0.75	0.75				
F-f	1.05	1.05	0.83	0.83				

$MMOH_{red}$

	docked to Mc			
	all atoms		heavy atoms	
	$S_{max} = 4$	$M_S = 0$	$S_{max} = 4$	$M_S = 0$
A	0.61	0.61	0.39	0.39
B	0.59	0.59	0.38	0.38
C	0.59	0.59	0.38	0.38

[a] For comparison, the active site of the Mc protein was RMSD docked to the active site of the Mt protein. When all atoms were included in the fitting algorithm, a value of 0.55 Å was recorded. Excluding the H atoms reduced the calculated RMSD value to 0.26 Å.

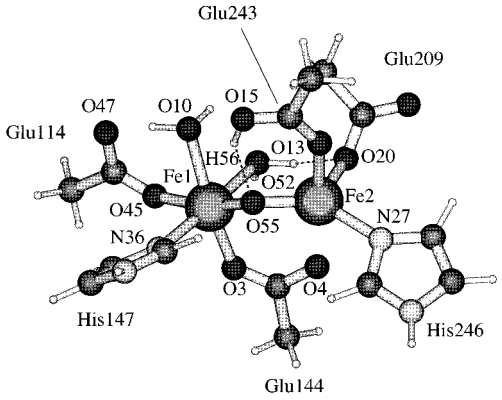

Figure 3. Optimized structure of $MMOH_{ox}$ model A cluster. In the oxidized model B cluster, the proton is on O55 instead of O15.

a. Models A and B. The optimized model A cluster is shown in Figure 3. Generally, the calculated Fe−Fe, Fe−N, and Fe−O distances compare fairly well with the experimental data (Table 4). Where deviations occur, they are within the effective experimental bond length uncertainties given the resolution of the X-ray data when estimated standard deviations of 0.20 Å or more are taken into account. The largest difference between calculated and observed geometric parameters arises in the vicinity of the $Fe_2\mu(H_2O)\mu(OH)\mu(CO_2)$ core, particularly for the bridging Wat666(OH^-) group. Here, the "open" or non-metal-coordinated oxygen atom of the Glu243 residue forms a (O15)Glu243.Oϵ1···H−Wat666(O55) hydrogen bond.[34] This hydrogen bond is so strong that the proton of Wat666(OH^-) is completely transferred to the Glu243.Oϵ1(O15) atom. An O^{2-} species is calculated to be one of the bridging ligands, rather than the OH^- alternative. In synthetic model complexes, bridging O^{2-} ligands typically have $Fe^{3+}-O^{2-}$ bond lengths in the range 1.7−1.9 Å,[5b,35] in fairly close agreement with the calculated $Fe^{3+}-O^{2-}$ distances of 1.77 and 1.80 Å in Table 4. A comparison with the protein X-ray data for Mc and Mt indicates one bridging Fe1−O55 distance within this range, while the Fe2−O55 distance is more in accord with the accepted range for $Fe^{3+}-OH^-$ bond distances observed in model systems of 1.9−2.1 Å.[36] Structural studies of both the Mc and Mt proteins suggest that Glu243.Oϵ1(O15) should be within hydrogen-bonding distance to Wat667(O10), but this appears insufficient to prevent proton transfer from occurring. The presence of an O^{2-} bridging ligand from our calculations rather than an OH^- ligand is inconsistent with electronic absorption, magnetic, and Mössbauer data which exclude the presence of an O^{2-} bridging ligand for $MMOH_{ox}$. From the X-ray data of the Mc protein, even with uncertainties taken into account for the estimated standard deviations in bond lengths of 0.20 Å,[5a] the Fe−Wat784(O52) bond lengths suggest that Wat784(O52) is weakly coordinated, but with a distinctly shorter bond to Fe1 than Fe2 (2.34 Å versus 2.55 Å averaged over protomers A and B), and this same trend is also observed in the calculations. In the Mt protein, however, both the observed Fe1−Wat(O52) and Fe2−Wat(O52) distances are much shorter than in Mc, and they are nearly equal. The source of this discrepancy will be addressed in the model D and E sections.

Optimized parameters for our model B quantum cluster are given in Table 4. For model B, the Wat666(O55)−H56 distance is constrained to ∼1.0 Å, and thus proton transfer to the Glu243.Oϵ1(O15) atom is artificially prevented. Calculated Fe−N and Fe−O values are mostly consistent with those observed for model A, with the exception of the Fe2−Glu243.Oϵ2(O13) distance. This bond shortens significantly from 2.09 Å (dative bond) in model A to 1.93 Å (covalent interaction) in model B. Alternatively, electrostatic charge transfer almost

(34) To describe this hydrogen bond accurately, the following convention is adopted in this manuscript so that the experimental and quantum descriptions of a hydrogen bond can be used interchangeably. When referring to the X-ray data, the conventional name of the protein residue + atom or solvent ligand corresponding to those in Figure 2a will be used, i.e., Glu243.Oϵ1. For ease of reference to the quantum cluster, as in Figure 3, the atom numbers as defined in the related ADF calculation will also be depicted in parentheses, i.e., (O15). Thus, Glu243.Oϵ1 in Figure 2a is identical to (O15) in Figure 3.

(35) Kurtz, D. M., Jr. *Chem. Rev.* **1990**, *90*, 585.
(36) (a) Armstrong, W. H.; Lippard, S. J. *J. Am. Chem. Soc.* **1984**, *106*, 4632. (b) Zang, Y.; Pan, G.; Que, L., Jr.; Fox, B. G.; Münck, E. *J. Am. Chem. Soc.* **1994**, *116*, 3653.

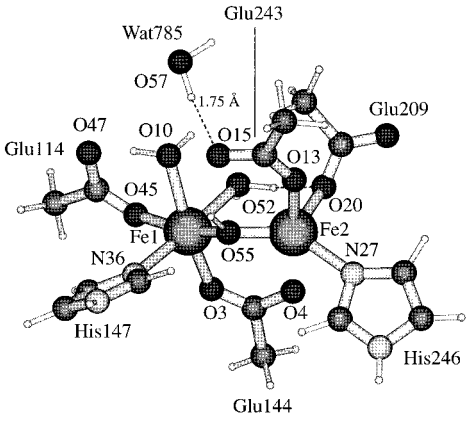

Figure 4. Optimized structure of $MMOH_{ox}$ model C cluster (tautomer I). Model C is produced by augmenting the model A or B cluster with an additional Wat785(O57) from the 1MTY data.

certainly plays a role and may be used to rationalize the trend in Glu243.Oϵ2(O13)−Fe2 distances, in that there is a competition from H^+ with Fe^{3+} for the OCO^- electron density. Energetically, model A is noted to be 15 kcal/mol more stable in energy than model B, suggesting that although the geometry appears insensitive to the proton redistribution, the related energetics are not and there is considerable stabilization associated with the protonation of Glu243.Oϵ1(O15). Such a difference in energy may imply a mechanistic role in the conversion between oxidized and two-electron-reduced forms of the enzyme where electron addition and coupled protonation is a requirement.

b. Model C. The active site is buried deep in the protein and surrounded by several possible hydrogen-bonding partners, which can include atoms from the first-shell ligands as well as the amino acid protein residues and solvent-based ligands in the second shell, all of which serve to tie up and saturate atoms with coordination vacancies. In the gas phase, without the presence of the extended environment, internal proton transfer becomes a distinct possibility. The tendency for protons to migrate to areas of high electron density has also been observed in calculations of manganese superoxide dismutase, where the effects of the environment are also not included.[37] Analysis of the Mc (and Mt) protein structure indicates that Glu243.Oϵ1 is in fact also hydrogen bonded to a H_2O molecule that lies in the second coordination shell, denoted Wat785 (from the Mc data, Figure 2a). In an attempt to better understand the factors that influence the intramolecular proton transfer mechanism, the second-shell Wat785 is included in our model C cluster. The water was placed at a (O15)Glu243.Oϵ1···H−Wat785(O57) hydrogen-bonding distance of 2.76 Å between the donor (O57) and acceptor (O15) atoms, as observed in the X-ray data. Model C is thus similar to model B but with an additional water incorporated into the cluster rather than a geometric constraint. The results for the model C calculation are also shown in Table 4 (column C(tI)), and the optimized structure is shown in Figure 4. From the calculation, the most important point to emerge is that the internal proton transfer that was observed in model A is prevented when Wat785 is present in model C, even though the proton has the complete freedom to transfer. Adding the second-shell Wat785 therefore adds an element of control to the intramolecular proton transfer mechanism. The distances of ligands coordinated terminally to the Fe centers closely resemble those calculated for model B: those associated with the O atoms of the bridging Wat (either H_2O or OH^-) and RCO_2-type ligands, such as the Fe1−Wat666(O55) and Fe2−Wat784(O52) distances, are calculated to be larger than those of model B by approximately 0.1 Å. Correspondingly, the calculated Fe−Fe distance of 3.34 Å is also 0.15 Å longer than that calculated for model B and approximately 0.2 Å longer than observed experimentally, a feature attributed to the addition of the second-shell Wat785 molecule. Nevertheless, the inclusion of Wat784 yields a similar RMSD of 1.00 Å fitted over all atoms (0.75 Å, heavy atoms only) for the BS calculation (Table 5).

The inclusion of Wat785 in the model C cluster clearly prevents the transfer of the bridging proton from Wat666(OH^-) to Glu243.Oϵ1(O15). Quantum geometry optimization, however, yields only a *local* and not a *global* minimum, in general. Therefore, the converse question can also be asked, "if Glu243.Oϵ1(O15) is protonated originally, does the proton revert back to Wat666 in the presence of Wat785?" In Table 4 (column C(tII)), the structure is reported for a second tautomeric form of model C where Glu243.Oϵ1(O15) is protonated. For model C tautomer II, in the presence of the Wat785, there is no observed intramolecular proton movement back to Wat666-(O55). Although Glu243.Oϵ1(O15) being protonated provides 1.2 kcal/mol of stability for tautomer II of model C, relative to tautomer I, the two tautomeric forms are nearly equienergetic. Compared to models A and B, where the energetic difference amounted to 15 kcal/mol, the inclusion of Wat785 strongly lowers the energetic difference (and probably also the barrier) for interconversion of these isomers. This may point toward a possible pathway by which the transfer of protons from the surrounding environment to the active site experiences no energetic disadvantage.

c. Model D. Model D differs from models A, B, and C in two respects. First, the protonation state of the bridging Wat784-(O52) of the $Fe_2\mu(OH)\mu(OH)\mu(CO_2)$ core is different, with 2 OH^- ligands replacing what was formally 1 OH^- and 1 H_2O as bridging ligands. This produces a number of geometric effects as discussed below. Second, changing the protonation state of the bridging ligands changes the overall charge of the quantum cluster, from +1 to neutral (Table 1). This may have important ramifications for the first step of the catalytic cycle, where two-electron reduction and coupled protonation results in a significantly rearranged $MMOH_{red}$ cluster, also of zero net charge. This therefore makes the $MMOH_{ox}$ to $MMOH_{red}$ conversion conceptually simpler in terms of overall charge change. The calculated Fe−N and Fe−O bond lengths are shown in Table 4 for model D, and the optimized structure is shown in Figure 5. The Fe−Fe distance of 3.11 Å and Fe2−Wat(O52) distance of 2.16 Å for model D are calculated significantly shorter than for models A (Fe−Fe = 3.13 Å, Fe2−O52 = 3.24 Å), B (Fe−Fe = 3.19 Å, Fe2−O52 = 3.28 Å), C (tautomer I) (Fe−Fe = 3.34 Å, Fe2−O52 = 3.41 Å), and C (tautomer II) (Fe−Fe = 3.17 Å, Fe2−O52 = 3.28 Å) consistent with the presence of $2OH^-$ ligands in the bridging positions. This matches the observed trend for these parameters in the X-ray data, where the Fe−Fe and Fe2−Wat distances in Mt (Fe−Fe = 2.99 Å, Fe2−O52 = 2.17 Å) are shorter than their corresponding parameters in either protomer of Mc (Fe−Fe = 3.04 Å, Fe2−O52 = 2.54 Å). Fe1−Wat(O52) is also predicted to be shorter in model D (2.01 Å) than in models A−C (2.25−2.29 Å). This is consistent with the observed experimental shortening of this bond comparing Mc (2.43 and 2.24 Å for protomers A and B, respectively) with Mt (2.15 Å). As

(37) (a) Li, J.; Fisher, C. L.; Konecny, R.; Bashford, D. Noodleman, L. *Inorg. Chem.* **1999**, *38*, 929. (b) Han, W.-G.; Lovell, T.; Noodleman, L. *Inorg. Chem.*, in press.

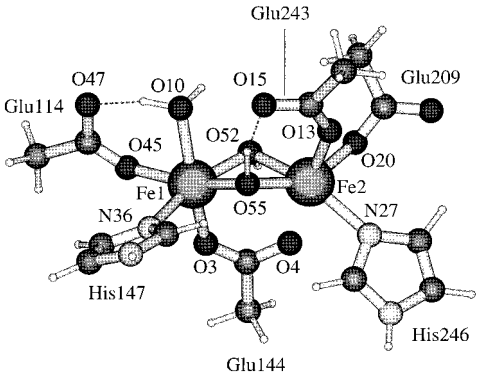

Figure 5. Optimized structure of $MMOH_{ox}$ model D cluster.[22a] Model D is produced from the model A or B cluster by removal of a proton residing on Wat784(O52).

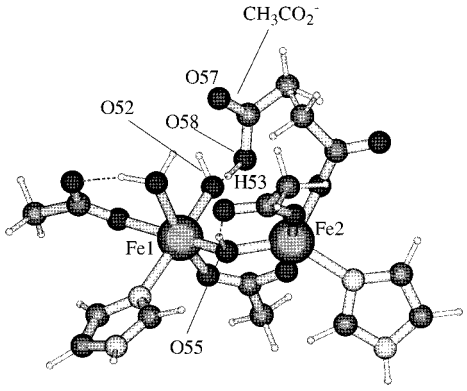

Figure 6. Fully optimized structure of $MMOH_{ox}$ model E cluster.[22a] Model E is produced by augmenting the model A or B cluster with an additional acetate (O57, O58)) from the 1MTY data.

a general observation, the geometry of the model D core (and models A, B, and C also) is insensitive to whether an AF or F alignment of electron spins is used, evident from the BS and HS geometries having identical RMSD values of 0.75 Å, 0.68 Å (heavy atoms only) and 0.89 Å, 0.90 Å (all atoms) docked to Mc and Mt, respectively. These heavy atom RMSDs indicate that model D is a better match to the Mt structure than to Mc, in agreement with the bond length trends discussed above.

d. Models E and F. The addition of the acetate ligand to model B produces our model E structure and changes the total charge on the active site cluster from +1 to 0 (Table 1). The charged acetate ion was added to the optimized model B cluster geometry at a position that most closely resembled its original position relative to the active site in the Mc X-ray data. Calculations for the model E cluster were implemented in two different ways. First, the position of the acetate (see Figure 2a) and its effect on the bridging Wat784 were allowed to vary only. The remainder of the cluster was constrained to that of the optimized model B geometry. In the second calculation, both the cluster and the acetate positions were optimized. These two different calculations are referred to as model E-partial and model E-full, and the optimized structure of the latter is shown in Figure 6. The model E-partial and model E-full geometries are summarized in Table 4. Both display geometries similar to that of model B, the largest discrepancy for model E-partial arising in the Fe1−O52 bond length, which is calculated shorter by approximately 0.23 Å compared to model B. AcO−Wat784 distances are also calculated to be shorter ($AcO_1\cdots O$ = 2.51 Å, $AcO_2\cdots O$ = 2.51 Å) than those noted in the X-ray data ($AcO_1\cdots O$ = 2.60 Å, $AcO_2\cdots O$ = 2.90 Å) by approximately 0.09 and 0.40 Å.

The model E-full structure differs from model E-partial and model B in that the AcO distances ($AcO_1\cdots O$ = 2.76 Å, $AcO_2\cdots O$ = 2.53 Å) are no longer identical[38] and there is a calculated internal proton transfer from Wat784 to AcO_2 (Figure 6). The proton transfer is interesting in the context of the real enzyme, because it suggests that the system not be described in terms of charged acetate ion and charged cluster. Instead, a more accurate description is a neutral acetic acid linked to a neutral diiron active site by a short strong asymmetric hydrogen bond with AcO_2-H = 1.03 Å, $Wat784\cdots H$ = 1.53 Å. Model E-full is calculated more stable than model E-partial by 13 kcal/mol, with a significant portion of this energy difference arising from the additional effects of geometric relaxation. The heavy atom RMSD for model E-full (0.75 Å) also compares better to the Mc protein data than model E-partial (1.12 Å).

The addition of the acetate ion to model D produces our model F structure (Table 1). Calculations on the model F cluster were also completed in a manner similar to those for the model E cluster, referred to as model F-partial and model F-full, and their respective geometries are summarized in Table 4. For model F-partial, the major changes to the active site occur for the Fe1−O52, Fe1−O55, and Fe2−O52 bond lengths. For model F-full, the calculations also produce an internal proton transfer from Wat784 to AcO_2 in which the proton is evenly shared ($AcO_2\cdots H$ = 1.15 Å, $Wat784\cdots H$ = 1.27 Å). All of these calculated bond lengths differ significantly from the Mc and Mt experimental geometries, and the other cluster models, particularly model E-full for the larger clusters, are a better match to the experimental structures (see Tables 4 and 5).

ii. $MMOH_{red}$. Calculated interatomic distances for our $MMOH_{red}$ quantum clusters are given in Table 6 along with the accompanying X-ray structural data for the characterized Mc protein. The calculated geometries are RMSD matched against the experimental parameters in Table 5.

a. Models A and B. The optimized model A cluster is shown in Figure 7. The calculation of the two-electron-reduced state of the enzyme reproduces the experimental coordinates with reasonable accuracy, for most bond lengths, angles, and torsions. The calculated Fe−Fe distance is a little long (Fe−Fe = 3.46 Å) but within the bounds of any experimental errors present in the X-ray data (standard deviation = 0.25 Å) or in the density functional. Most importantly, the structure of the novel μ-1,1 Glu243.Oϵ1(O13) bridge is preserved, with the largest errors arising in the positions of the imidazole rings and the carboxylate-type ligands coordinated terminally to the Fe sites. The deviation from the experimental geometry is most pronounced for Glu209, where the calculated Glu209.Oϵ2(O20)−Fe2−Fe1 angle of 135° is larger by 13°. From the recent analysis of Dunietz et al.,[21m] an extra water not located in the original X-ray assignment has been identified from a reevaluation of the electron density map of $MMOH_{red}$ and is designated the hydrogen-bonding partner to Glu209.Oϵ1(O22). The inclusion of this extra water in our model B cluster appears to have little effect on the geometry of the active site. Similar discrepancies in the orientation and position of the protein amino acid side chains were also observed between the X-ray data and our $MMOH_{ox}$ cluster calculations. No difference between BS and HS calculations was observed when the optimized $MMOH_{red}$ model A structure was RMSD fitted against the X-ray data of the Mc protein, with values of 0.61 Å (all atoms) and 0.39 Å

(38) The calculated AcO···O distances are now the reverse of that seen in the real enzyme in which $AcO_1 < AcO_2$. It is therefore likely that there are two distinct solutions in which either AcO_1 or AcO_2 may be protonated. We have only calculated one possibility.

Table 6. Calculated and Experimental Interatomic Distances (Å) for $MMOH_{red}$

			active site model						Mc	
			A[a]		B[b]		C[c]			
atom	atom	ligand type	AF	F	AF	F	AF	F	prot. A (red.)[d]	prot. B (mixed ox./red.)[d]
Fe1	Fe2		3.46	3.46	3.44	3.44	3.39	3.38	3.28	3.43
Fe1	O45	O_t	2.07	2.07	2.08	2.08	2.05	2.05	1.90	1.93
Fe1	N36	N_t	2.15	2.15	2.15	2.15	2.19	2.19	2.39	2.31
Fe1	O3	μCO_2	2.13	2.13	2.11	2.12	2.11	2.10	2.15	2.00
Fe1	O55	n/a	n/a	n/a	n/a	n/a	n/a	n/a	n/a	1.56
Fe1	O10	O_t	2.23	2.23	2.22	2.22	2.27	2.27	2.63	n/a
Fe1	O52	O_t	2.34	2.34	2.35	2.33	2.38	2.38	1.92	n/a
Fe1	O13	di-μO	2.18	2.18	2.17	2.19	2.15	2.16	2.10	2.67
Fe2	O20	O_t	1.91	1.91	1.91	1.91	1.93	1.93	2.27	1.86
Fe2	N27	N_t	2.12	2.12	2.12	2.12	2.14	2.14	1.94	2.07
Fe2	O13	di-μO	2.18	2.18	2.19	2.18	2.27	2.27	2.33	n/a
Fe2	O15	O_t	2.25	2.25	2.25	2.25	2.30	2.29	2.33	1.97
Fe2	O4	μCO_2	2.39	2.39	2.39	2.39	2.40	2.39	2.39	2.26
Fe2	O55	μO	n/a	n/a	n/a	n/a	n/a	n/a	n/a	2.23
Fe2	O52	O_t	2.94	2.94	2.95	2.96	2.39	2.38	2.72	2.52
O10	O47		2.52	2.52	2.52	2.52	2.49	2.49	2.92	2.65
O10	O52		2.87	2.87	2.86	2.85	3.20	3.20	2.60	n/a
$O55^B$	O22		n/a	n/a	3.00	3.00	3.00	3.00	n/a	n/a

[a] A: Active site model from protein X-ray data. [b] B: Extra H_2O assigned to model A cluster to H-bond and saturate Glu209.Oϵ1. [c] C: Additional second-shell Wat858 assigned to model B cluster. [d] Protomers A and B are the two crystallographically independent halves of the $\alpha_2\beta_2\gamma_2$ hydroxylase dimer of Mc, for which standard deviations in the experimental bond lengths are ~0.25 Å, ref 5a. Protomer A is the chemically reduced diiron center. Protomer B corresponds to an oxidized or partially reduced diiron center.

(heavy atoms only) suggesting an excellent overall matching of calculation with experiment.

The reported X-ray bond lengths in Table 6 raise an interesting issue. For protomer A of Mc, both the spectroscopy and X-ray evidence point toward Fe1 being 5-coordinate; however, the coordination environment around Fe2 is less clear-cut. The spectroscopy shows Fe2 having five ligands coordinated, while the single crystal X-ray data suggests that four ligands are bound to Fe2, but only when the assumption holds that the Fe2−O4 interaction remains weak. Our calculations predict that Fe1 should be surrounded by an approximately octahedral array of six ligands, whereas on the basis of the large Fe2−Glu144.Oϵ1(O4) distance of 2.39 Å, four ligands appear covalently bound to Fe2. For $MMOH_{red}$, a feature of the active site not reproduced by the calculations is the position of the axially coordinated Wat856(O10) molecule, experimentally observed as weakly bound to Fe1. Even though the optimization for the model A cluster was started with weak coordination for this ligand, strong association was calculated compared with that in the X-ray data. On the basis of a structural analysis alone, the reasons for this preference are not clear. One possible rationale may involve the first-shell Glu114.Oϵ2(O47), which forms a reasonable hydrogen bond with Wat856(O10). The combined effect of the hydrogen bond to Glu114.Oϵ2 coupled with the correct orientation of the Wat856 dipole and the vacant coordination site at Fe1 is to pull Wat856(O10) back into the first shell, where it coordinates to Fe1. The calculated Fe1−Wat856(O10) distance of 2.23 Å is therefore much shorter than the 2.63 Å observed experimentally. Importantly, even when the water dipole is inverted and unfavorably oriented for an interaction with Fe1, the dipole reorients and strong association persists in the calculations.

In the Mc protein, the nearest residue to Wat856(O10) is the second-shell threonine residue, Thr213, which lies ~5 Å from Wat856. This is too far to form even a weak hydrogen bond. However, gaps in the protein hydrogen-bonding network can be compensated for by solvent molecules that fill the open channels. A second-shell water molecule, Wat858, sits in the channel between the Thr213.Oγ1 atom and Wat856 (Figure 2b). Wat858 participates in two important hydrogen bonds. The first arises because Wat858 lies within 2.6 Å of Thr213.Oγ1 and thus forms a strong Thr213.Oγ1···H−Wat858 hydrogen bond. The second hydrogen bond is to Wat856(O10), which lies within a distance of 3.2 Å, and this (O10)Wat856···H···Wat858(O58) hydrogen bond is typically very strong. Wat858 and Thr213 may be the key elements of the protein and solvent hydrogen-bonding network that ensure that Fe1−Wat856(O10) is weakly coordinated (see model C below).

b. Model C. The position of the Wat856(O10) molecule, which was inaccurately represented in the smaller model A calculations, is the central focus of our model C cluster calculations. To address the problem of the position of the weakly bound Wat856(O10), a second-shell water molecule, Wat858(O58), which is the hydrogen bond partner to Wat856, is incorporated into the active site model and its position fixed at a distance of 4.23 Å relative to Fe1, this value corresponding to that observed in the X-ray data. The dipoles of the structurally characterized waters were correctly oriented to maximize hydrogen-bonding interactions between them. The working hypothesis was that the hydrogen bond between Wat858(O58) and Wat856(O10) would be strong enough to prevent Wat856-(O10) from further recoordinating to Fe1, and only with the inclusion of Wat858 and its hydrogen bond partner would it be possible to reproduce a longer Fe1−Wat856(O10) distance similar to that observed in the X-ray coordinates. However, even with the inclusion of the second-shell Wat858(O58) into our model C cluster, the optimized geometry (Table 6) did not reproduce the weak coordination associated with Wat856(O10). This discrepancy in Fe−Wat856 bond length has seemingly gone unnoticed in other DFT studies of MMO and may simply reflect the inadequacies in the quantum models. Alternatively, if the gas phase calculations predict Wat856 to be strongly bound, but the X-ray data and spectroscopy support a weakly bound Wat856, then what prevents Wat856 from being strongly coordinated to Fe1? The protein and solvent environment may play an undescribed role in the simple gas phase calculations. Simply put, the environment may raise the energetic penalty incurred as Wat856(O10) begins to associate with Fe1, and this

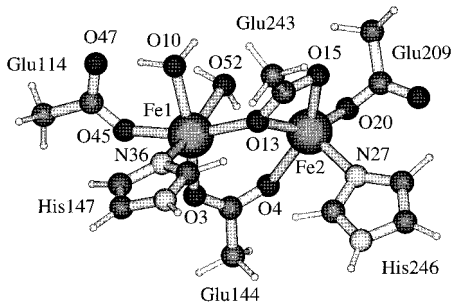

Figure 7. Optimized structure of $MMOH_{red}$ model A cluster.

cannot be described geometrically and, more importantly, energetically, with calculations that do not take protein effects into account. The linear transit pathway describing the motion of Wat856, from weak association to strong covalent interaction as a function of Fe1−Wat856(O10) distance, is described in more detail in a separate publication along with the accompanying energetics imposed by the protein and solvent environment.[22b]

The positions of the weakly associated Wat856(O10) and the more strongly Fe1-linked Wat860(O52) in the experimental Mc structure[5a] are also interesting in the context of the docking of component B to $MMOH_{red}$, and MMO function in general. The rate with which $MMOH_{red}$ reacts with molecular O_2 is significantly enhanced when MMOB docks to MMOH.[39] Spectroscopic studies propose that the docking of component B results in an as-yet unknown structural rearrangement of the diferrous core which leads to an enhancement in rate. It may follow that the lability of the weakly associated Wat856 plays a major role in the structural rearrangement of the diiron core, the weakly associated and entropically favored form allowing the proposed structural reorganization, while the strongly coordinated and entropically disfavored form does not. A comparison of the structures of the diferrous forms of the diiron proteins in Figure 1 is also instructive, suggesting a possible role for Wat856 in $MMOH_{red}$ and reasons for the structural differences observed between $MMOH_{red}$ and its two diiron counterparts. The diferrous form of RNR is the only diferrous state not requiring a structural rearrangement for enhanced reaction with molecular O_2. MMOH requires MMOB docking; Δ^9D requires that ACP-stearoyl substrate be bound. In MMOH, before component B docks, the presence of the associated Wat856 and Wat860 (Figures 2b and 7) drives the quite novel coordination of the Glu243 side chain on both geometric and electrostatic grounds and prevents the more conventional μ-1,3 bidentate bridging mode, noted in RNR and Δ^9D, from being attained. The lability of the Fe−Wat856 bond may imply that, upon component B docking, Wat856 could move in or out as required to accommodate an alternative orientation of Glu243. Subtle changes in the coordination of Glu side chains have already been noted to have dramatic effects on the geometry of the active site for other altered (D84E RNR, Y122F N_3^- bound RNR)[40,41] non-heme diiron proteins.

The majority of theoretical studies of MMO have thus far focused on the identity of the key catalytic intermediates, the diiron(III,III) peroxo and the high-valent diiron(IV,IV) species, and a more complete description of the catalytic pathway up to the reaction of the high-valent intermediate with methane substrate. Consequently, comparison of this work with studies

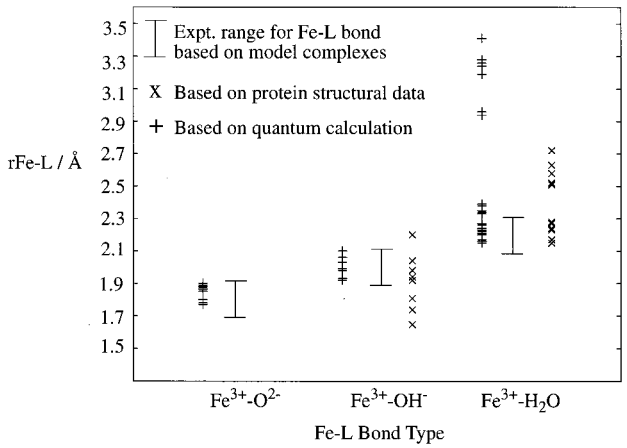

Figure 8. Scatter plot comparing calculated (+) Fe^{3+}−L bonds (L = O^{2-}, OH^-, H_2O) with the experimental (×) data found in $MMOH_{ox}$. The experimental range of Fe^{3+}−L bonds was obtained from X-ray structures of synthetic model systems.[35]

of a similar focus is limited. The recent paper by Dunietz et al.[21m] provides the greatest scope for immediate overlap. Generally, our calculated geometries and *J* values for the $MMOH_{ox}$ cluster models are similar to that calculated with their small (∼60 atoms) and larger cluster (100 atoms or more, in which there are a number of second-shell ligands) models. For the reduced form, models A, B, and C of this work provide excellent representations of the X-ray data; only for a much larger cluster is their structure for $MMOH_{red}$ reasonable. Notable discrepancies between calculated and experimental results for $MMOH_{red}$ arise in the position of the weakly bound Wat856 that lies in the second coordination sphere and that of the bridging Wat860. Even for their large $MMOH_{red}$ cluster, the positions of these waters in the Dunietz et al. results deviate from those seen in the reduced Mc X-ray structure. Wat856 is calculated to be strongly covalently bound to Fe1 (2.21 Å), a value which agrees well with our results (2.33−2.27 Å), while the X-ray coordinates suggest that Wat856−Fe1 = 2.63 Å, substantially different from the calculations, the possible reasons for which have been noted previously. The bridging Wat860 in their work is calculated to be weakly associated with both Fe sites (Wat860−Fe1 = 2.80 Å, Wat860−Fe2 = 2.75 Å), notably different from the Wat860−Fe1 = 1.92 Å and Wat860−Fe2 = 2.72 Å distances found in the protein data for the chemically reduced form of the enzyme and our calculations (Fe1−O52 = 2.34−2.38 Å, Fe2−O52 = 2.38−2.96 Å) (Table 6).

2. Statistical Evaluation of Fe−O Bonds. In a variety of synthetic model complexes, bridging O^{2-} ligands typically have Fe^{3+}−O^{2-} bond lengths ranging from 1.7 to 1.9 Å, whereas the corresponding ranges of bond lengths[35] for Fe^{3+}−OH^- and Fe^{3+}−H_2O bridging ligands are 1.9−2.1 and 2.1−2.3 Å, respectively. The protonation state of the oxygen-based bridging ligands can therefore usually be distinguished on the basis of bond length. DFT calculated bond lengths reported in Table 4 for $MMOH_{ox}$ are plotted using the above distance criteria for the model complexes as an indication of protonation state of the oxygen-based ligands in Figure 8. Thus, distances that appear in the 1.7−1.9, 1.9−2.1, and 2.1−2.3 Å ranges are plotted in their respective Fe^{3+}−O^{2-}, Fe^{3+}−OH^-, and Fe^{3+}−H_2O regimes. The data from both proteins are also incorporated on the basis of their assigned protonation state from the X-ray analyses. Figure 8 therefore easily allows a comparison of calculated (+) Fe^{3+}−L (L = O^{2-}, OH^-, or H_2O) values with experimentally reported values (×) from the $MMOH_{ox}$ single-crystal data.

(39) Pulver, S. C.; Froland, W. A.; Lipscomb, J. D.; Solomon, E. I. *J. Am. Chem. Soc.* **1997**, *119*, 387.
(40) Voegtli, W. C.; Khidekel, N.; Baldwin, J.; Ley, B. A.; Bollinger, J. M., Jr.; Rosenzweig, A. C. *J. Am. Chem. Soc.* **2000**, *122*, 3255.
(41) Andersson, M. E.; Högbom, M.; Rinaldo-Matthis, A.; Andersson, K. K.; Sjöberg, B.-M.; Nordlund, P. *J. Am. Chem. Soc.* **1999**, *121*, 2346.

Table 7. Calculated Energies and *J* Values of Active Site Quantum Cluster Models for $MMOH_{ox}$ and $MMOH_{red}$

	$MMOH_{ox}$[a]									$MMOH_{red}$[b]			
	A[c]	B[d]	C(tI)[e]	C(tII)	D[f]	E-p[g]	E-f	F-p[h]	F-f	A	B[i]	C[j]	units
opt. geometry													
HS	−339.3	−338.9	−353.8	−353.5	−341.0	−386.8	−387.4	−386.0	−386.3	−334.3204	−348.8057	−363.5680	eV
BS	−339.9	−339.2	−354.0	−354.0	−341.1	−387.1	−387.7	−386.1	−386.4	−334.3180	−348.7932	−363.5681	eV
$E_{HS} - E_{BS}$	14.8	7.4	3.7	11.9	2.1	6.3	5.2	1.8	3.4	−0.06	−0.3	0.0023	kcal/mol
J(calc)[k]	−206	−104	−52	−167	−29	−88	−72	−25	−47.6	+1.2	+6.3	−0.8	cm^{-1}
J[l]	−142	−90	−30	−109.2	−11	−90	−39.2	−23	−42.7				
J[m]	−185	−145	−79	−116.7	−69	−155	−203.7	−218	−335.3				
X-ray geometry		Mc			Mt						Mc		
HS		−336.1			−329.4						−332.2		eV
BS		−336.3			−329.5						−332.1		eV
$E_{HS} - E_{BS}$		4.6			2.5						1.5		kcal/mol
J(calc)[k]		−64			−35						+32		cm^{-1}
J(expt)[n]					−4 to −10						+0.35		

[a] $S_{max} = 5$. [b] $S_{max} = 4$. [c] H_2O/OH^- model with internal proton transfer from the bridging $[O-H]^-$ to Glu243Oϵ1. [d] H_2O/OH^- model with no proton transfer. [e] H_2O/OH^- model with extra water. [f] $2OH^-$ model. [g] Model B cluster + $CH_3CO_2^-$. [h] Model D cluster + $CH_3CO_2^-$. [i] Extra water H-bonded to Glu209.Oϵ2.[10m] [j] 2 extra waters added to $MMOH_{red}$ model A. [k] Calculated adiabatically using the formalism $E_{HS} - E_{BS} = -S_{max}^2 J$. [l] $J = Ae^{-BP}$ ($A = 8.763 \times 10^{11}$ cm^{-1}, $B = 12.663$ $Å^{-1}$).[42b] [m] $J = 1.337 \times 10^8(3.536 + 2.488 \cos\phi + \cos^2\phi) \times e^{-7.909r}$.[42a] [n] Values reported for the Mt protein using the convention $H = -2J\vec{S}_1\cdot\vec{S}_2$.[3b]

Two important features emerge from Figure 8. First, the character of a particular solvent-derived ligand can be predicted well on the basis of its bond length to Fe from the quantum calculations. For the most part, calculated values of $Fe^{3+}-O^{2-}$, $Fe^{3+}-OH^-$, or $Fe^{3+}-H_2O$ are in excellent accord with the standard or typical experimental ranges noted previously for the model complexes. Notable exceptions are the weakly coordinated terminal aquo ligands and their bridging counterpart where one component of the $Fe^{3+}-H_2O-Fe^{3+}$ bond of the bridge is long and the other short, giving rise to a noncoordinated $Fe^{3+}-H_2O$ interaction. The second point is that three of the experimentally assigned bond lengths in the $MMOH_{ox}$ crystal structures are inconsistent with the range of distances normally associated with $Fe^{3+}-OH^-$ bonds. These distances of 1.62, 1.78, and 1.71 Å are much shorter and, on the basis of distance criteria alone, would be better placed in the $Fe^{3+}-O^{2-}$ regime, a feature duly noted by the authors of the structural analyses in both cases. In the context of the other non-heme diiron proteins, bridging $Fe^{3+}-O^{2-}-Fe^{3+}$ interactions have been noted for RNR_{ox} and Δ^9D_{ox}. However, the presence of O^{2-} ligands in $MMOH_{ox}$ has been fairly conclusively discounted from spectroscopic evidence in that no optical signal is observed from the $MMOH_{ox}$ cluster in the anticipated spectral region for well-characterized O^{2-}-bridged diiron clusters. Furthermore, the measured exchange coupling constant for $MMOH_{ox}$ is much smaller than those noted for other model and native O^{2-}-bridged diiron clusters,[42] favoring $Fe^{3+}-OH^-$ interactions over $Fe^{3+}-O^{2-}$. Hence, the collective experimental perspective on $MMOH_{ox}$ indicates that O^{2-} character is absent and all solvent-derived ligands are either OH^-- or H_2O-based.

3. Gas-Phase Energetics of $MMOH_{ox}$ and $MMOH_{red}$ Model Clusters. In Table 7, gas phase energies for both F and AF spin states are shown, as well as the energy difference between the two spin alignments. For $MMOH_{ox}$, the AF state is calculated to be lower in energy than the F state in all cases. However, the energy difference between the AF and F states is only 2−15 kcal/mol so that *J* is fairly small. This suggests that in the enzyme excited spin states may be thermally populated relatively easily at low temperatures. Small differences in energy between AF and F states are also consistent with the experimental observation that an EPR signal from an $S = 2$ excited state is noted to maximize in intensity at around 30 K.[12d] For $MMOH_{red}$, the absolute energies indicate the reverse trend, with the F state lying below the AF state, although the two states are very nearly equal in energy. This low-energy F state in $MMOH_{red}$ may be functional for its reaction chemistry with molecular O_2 (a well-known spin triplet) if a concerted two-electron transfer mechanism is involved. Spin crossing from the AF to F state and population of redox-active Fe-based 3d orbitals having the correct orientation for reaction with O_2 is a likely prerequisite, and this is only achieved for the lowest-lying empty orbitals of the F state. These general observations for the energies of the F and AF states are consistent with those observed experimentally.

The trend in calculated total energy for a cluster at its optimized and X-ray geometries illustrates the necessity for geometry optimization. For $MMOH_{ox}$ model B and $MMOH_{ox}$ model D clusters, the RMSD docking (Table 5) of both optimized structures to the X-ray data suggests that the changes in geometry, in both cases, are only relatively minor but the optimized structures lie significantly stabilized in energy. Substantial differences in energy appear from only minor alterations in active site geometry. Since the precision of the X-ray data allows for variation in bond length of approximately ±(0.1−0.2) Å and one or several bond lengths assigned incorrectly can impose a substantial energetic penalty, such large energy differences between both optimized and X-ray structures are not surprising. At the optimized geometries, all the calculations are internally consistent and energetic comparisons between related states of a catalytic cycle are more meaningful.

4. Heisenberg Coupling Parameters. i. $MMOH_{ox}$. Spectroscopic studies have been an important tool for probing the nature of the bridging ligands of $MMOH_{ox}$. Optical absorption,[12c,13b] Mössbauer,[12d,13c] and Fe K-edge EXAFS[12f] measurements indicate that the bridging oxygen ligands are protonated. Parallel mode EPR revealed a small but sharp resonance ($g = 8.0$) which maximizes in intensity around 30 K, from which a measured *J* value is obtained for Mt in the range −4 to −10 cm^{-1}.[12d] This value is notably smaller than those of diiron proteins and model complexes[42] containing the $Fe^{3+}-O^{2-}-Fe^{3+}$ unit. Figure 9 (Table 7) compares adiabatically calculated Heisenberg coupling parameters both at the optimized geometries and at the experimental X-ray geometries (filled symbols in Figure 9) with their experimentally measured counterparts.

(42) (a) Weihe, H.; Güdel, H. U. *J. Am. Chem. Soc.* **1997**, *119*, 6539. (b) Gorun, S. M.; Lippard, S. J. *Inorg. Chem.* **1991**, *30*, 1625.

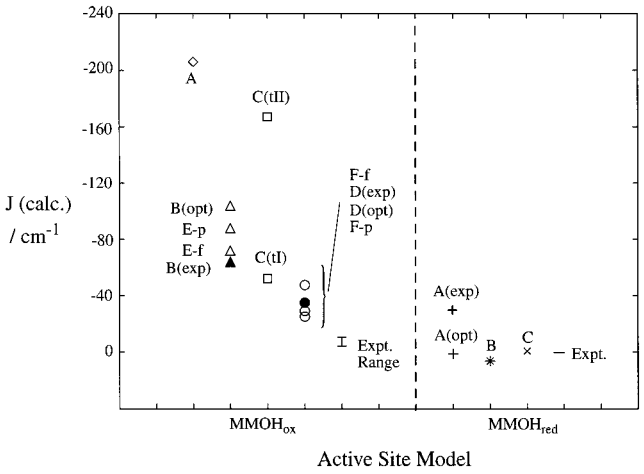

Figure 9. Comparison of calculated and experimental *J* values. Model cluster labels are arranged to correspond with the distribution of symbols.

For model A ($Fe^{3+}-O^{2-}(H_2O)-Fe^{3+}$ bridge), *J* is calculated to be comparatively large at -206 cm^{-1}. This value is typical for $Fe^{3+}-O^{2-}-Fe^{3+}$ containing complexes and indicative of the strong antiferromagnetic coupling seen for O^{2-}-bridged compared to OH^--bridged systems, and it is incompatible with the experimentally observed range of values for $MMOH_{ox}$ in Mt. For model B ($Fe^{3+}-OH^-(H_2O)-Fe^{3+}$ bridge), the calculated *J* falls to -104 cm^{-1}. Weaker coupling is therefore predicted between the two Fe sites in the model B cluster than in model A. For model C (tautomer I, $Fe^{3+}-OH^-(H_2O)-Fe^{3+}$ bridge), incorporation of Wat785(H_2O) decreases the calculated *J* value further to -52 cm^{-1} and closer to the absolute experimental range of values. For model C (tautomer II, $Fe^{3+}-O^{2-}(H_2O)-Fe^{3+}$ bridge), the larger value of -167 cm^{-1} lies closer to the regime of O^{2-}-bridged diiron systems and, as for model A, is largely inconsistent with experiment. For models A, B, and C, strong hydrogen bonding between Wat666(OH^-) and Glu243.Oϵ1 and the possibility for intramolecular proton transfer suggests that partial O^{2-}-type character may be present in Mc. At the very least, a tautomeric mixture as in model C (tautomers I and II) that includes partial O^{2-} character cannot be discounted.

For model D ($Fe^{3+}-(OH^-)_2-Fe^{3+}$ bridge), a calculated *J* value of -29 cm^{-1} is smaller than for models A, B, and C. The comparative trend in $Fe-L_{bridge}$ ($L_{bridge} = O^{2-}$, OH^-, H_2O) distances suggests that superexchange pathways by which electrons become delocalized from Fe1 to Fe2 and vice versa via the bridging oxygen-based ligands may well be the significant factor governing the magnitude of *J*. Notably, model D displays the largest average $Fe-L_{bridge}$ distance and the trend in *J* values for $MMOH_{ox}$ models A, B, C, and D varies inversely in accord with this parameter: the shorter the average $Fe-L_{bridge}$ distance, the larger, and therefore stronger, the calculated antiferromagnetic interaction. This calculated trend in *J* agrees well with the empirical correlation of Gorun and Lippard in which *J* was noted to vary as a function of the shortest $Fe-L_{bridge}$ pathway.[42b] Values of *J* reported in the literature are for the Elango ($Fe^{3+}-(OH^-)_2-Fe^{3+}$)[5b] structure ($J_{exp} = -7 \pm 3$ cm^{-1}, Mt protein) and, on the basis of a combined structural and magnetic property comparison of model C (tautomers I and II) and model D from our calculations with the X-ray geometry, is likely to contain either $Fe^{3+}-(OH^-)_2-Fe^{3+}$ or a mixture of $Fe^{3+}-(OH^-)_2-Fe^{3+}$ and $Fe^{3+}-OH^-(H_2O)-Fe^{3+}$.

Of the larger clusters, the full optimizations for models E and F are of most interest, primarily because of the involvement of intramolecular proton transfer in both cases. For model E-full, the calculated *J* value of -72 cm^{-1} is closer in agreement to the reported experimental range than either model E-partial ($J = -88$ cm^{-1}) or models A and B, but larger in comparison to model D. As noted previously, on complete proton transfer from Wat784 to the acetate ion, both the acetic acid and the now formally ($Fe^{3+}-(OH^-)_2-Fe^{3+}$) active site attain zero charge. The original proton abstracted by the acetate is then partially donated back to Wat784(OH^-) and is shared asymmetrically in a short but very strong O−H−O bond (Table 4). This back-donation and resultant unequal sharing of the proton raises *J* to a value higher than normally calculated for ($Fe^{3+}-(OH^-)_2-Fe^{3+}$) complexes. The structure of the model F-full cluster reveals that a similar proton abstraction (formally now $Fe^{3+}-O^{2-}(OH^-)-Fe^{3+}$) and back-donation mechanism is present and allows the low *J* value of -48 cm^{-1} to be rationalized on the basis of a more equal sharing of the back-donated proton (Table 4).

Table 7 also shows the correlation between the *J* values calculated from our DFT studies and those generated using empirical relationships derived from magnetostructural correlations based on a distance parameter alone (measuring the shortest superexchange pathway through the bridge) or a combination of angle and distance parameters for a large number of $Fe^{3+}-O^{2-}$ type model complexes.[42] The trend in our calculated *J* values using DFT maps well with those values of *J* expressed empirically as function of half the shortest $Fe-L_{bridge}$ superexchange pathway between the two ferric ions and suggests that the methodology is applicable to the study of ferric diiron ligand-bridged systems in general. A reduction in correlation with the DFT generated *J* values is noted when *J* is formulated with an angular and a distance dependence. $Fe-L_{bridge}$ bond lengths therefore appear to be the more influential component for the correlation.

ii. $MMOH_{red}$. The substantial decrease in exchange coupling upon two-electron reduction can be ascribed to several effects including the decrease in effective nuclear charges of the two Fe sites and the reduced Fe−ligand covalency. The coupling is thus very weak and mediated by the unusual μ-1,1 and μ1,3 carboxylate bridges. Other structural rearrangements for the two-electron-reduced $MMOH_{red}$ are noted to render the two Fe sites 5-coordinate and 6-coordinate, one site having a weakly coordinated axial water ligand. The gross change in structure is also accompanied by an AF to F spin transition, consistent with magnitude of the observed magnetic exchange coupling lying in the vicinity of the AF−F crossover, at about $+0.35$ cm^{-1}. The gas phase calculations for the AF and F states are approximately equienergetic, indicating that there is no energetic disadvantage associated with the AF to F spin crossing. The absolute sign and magnitude of the calculated *J* values for $MMOH_{red}$ cluster models A, B, and C are fully in accord with experimental measurements[14b] and well within the expected accuracy of the calculational method.

For both $MMOH_{ox}$ and $MMOH_{red}$ the calculated *J* coupling constants for the optimized geometries and those calculated for the single-crystal X-ray structure geometries are reasonable approximations to the experimental values both in sign and in magnitude. In fact, the calculated exchange coupling constants are rather good given the known tendency of DFT with general gradient corrections to overestimate *J* by a factor of about 2−3. *J* values of a similar magnitude have also been calculated for MMO[21m] and other non-heme diiron proteins[20f] using DFT methods, suggesting that the cluster models used to represent the active site are realistic in each case.

V. Conclusions

Over the past 10 years, only two of the physiologically relevant states of the MMO catalytic cycle ($MMOH_{ox}$ and $MMOH_{red}$) have been both structurally and spectroscopically characterized. For $MMOH_{ox}$, however, the protein X-ray data present a dilemma in that the identity of the oxygen-based bridging ligands appears different in the two available structures (from Mc and Mt) of the enzyme. In an effort to obtain molecular-level insight into the true nature of these bridging ligands and the early stages of the MMO catalytic cycle, structural and energetic aspects of the active site of $MMOH_{ox}$ and $MMOH_{red}$ have been examined. Using several quantum models, geometries of $MMOH_{ox}$ and $MMOH_{red}$ have been optimized using DFT methods. Calculated geometries are in good agreement with the reported X-ray data. In all cases, the geometries, particularly the metal−metal distances, which are greater than 3.0 Å, appear insensitive to the spin-coupling mode (AF or F) employed. Significantly, a number of bimetallic complexes are capable of binding molecular O_2 in its triplet ground state (the next step in the catalytic cycle of MMO) and the majority also have metal−metal separations in excess of 3.0 Å.[43]

Calculated Heisenberg spin coupling parameters are typically of the correct sign and magnitude for $MMOH_{ox}$ and $MMOH_{red}$ and in very good correspondence with that measured for the Mt protein. The DFT calculated J values for $Fe^{3+}-(L_{bridge})_2-Fe^{3+}$ ($L_{bridge} = O^{2-}$, OH^-, H_2O) also correlate well with the nature of the bridging ligands and bridge geometry, as shown by the good correspondence with the empirical equation for the shortest $Fe-L_{bridge}$ pathway. For $MMOH_{ox}$, AF coupling of electron spins on adjacent Fe sites is favored while AF and F spin coupling modes appear approximately equienergetic for $MMOH_{red}$. Small values of J for the latter form of the enzyme suggest that spin flipping between AF and F states will be accessible at room temperature, thereby giving rise to low-energy electron transfer pathways by which the process of reductive cleavage of the O−O bond may begin.

Although second-shell ligands are not directly covalently linked to the active site, they are indispensable for accurate energetic calculations. When Wat785 is excluded from the $MMOH_{ox}$ energetics, the proton-transferred model A cluster (μO^{2-}, μH_2O) is 15 kcal/mol more stable than the non-proton-transferred model B (μOH^-, μH_2O) alternative. Augmentation of the smaller model A and B clusters by a second-shell Wat785 molecule produces cluster model C and renders the non-proton-transferred and proton-transferred forms of model C approximately equienergetic. This is of major significance for the energetic balance between the two forms of model C and may be particularly relevant to the mechanism by which protons gain access to the active site during the early stages of enzyme turnover. Without the inclusion of Wat785, the stabilization associated with the model A cluster is overestimated relative to model B, and this situation is unlikely to be the case in the Mc or Mt enzyme.

From the combination of DFT calculated structures, gas phase energetics, and exchange coupling constants, the wealth of data now enable us to assess the identity of the bridging ligands in the two different $MMOH_{ox}$ protein X-ray data and the likely charge on the active site cluster. Of the smaller models that have been compared to the Mt protein, the matching of structural (RMSD = 0.75 Å) and magnetic properties ($J = -29$ cm^{-1}) of the model D cluster with the experimental data favors the 2μOH structure as the majority species. All other smaller models, such as models A, B, and C (tautomers I and II), have higher geometric RMSDs, and calculated J values (ranging from −206 to −52 cm^{-1}) do not reflect the experimental range (−4 to −10 cm^{-1}) as well. The dominant form of the $MMOH_{ox}$ active site in the Mt protein is therefore anticipated to contain $2\mu OH^-$ bridging ligands with a total cluster charge of 0. In the Mc protein, the presence of the exogenous $CH_3CO_2^-$ ion (only seen in the Mc bacterium) *must* be taken into account. Of the larger clusters, model E-full provides the best structural matching (RMSD = 0.75 Å) with the Mc X-ray data as well as giving a reasonable value of J (−72 cm^{-1}). Although the $CH_3CO_2^-$ ion is almost certainly a crystallization artifact derived from the NH_4OAc buffer, its very presence in the Mc protein suggests that $1H_2O$ and $1OH^-$ are initially present as the dominant bridging species. However, the DFT calculations suggest that the proton of the bridging Wat784 may be shared internally with the exogenous acetate and a more correct description would be a neutral acetic acid hydrogen bonded to a diiron unit displaying $2\mu OH^-$ bridging ligands and an overall cluster charge of 0. Of the smaller models, model C (tautomer I) is also quite reasonable both structurally (RMSD = 0.75 Å) and for magnetic properties ($J = -52$ cm^{-1}). By contrast, while model B (RMSD = 0.74 Å) and model C (tautomer II, RMSD = 0.75 Å) are comparable to model E-full in accuracy of RMSD fit, the calculated magnetic data for model B (−104 cm^{-1}) and model C (tautomer II, −167 cm^{-1}) are less convincing. J for $MMOH_{ox}$ in the Mc protein has not yet been measured, and this would clearly be very valuable to aid in the comparison.

Throughout the discussion of the geometries of the $MMOH_{ox}$ and $MMOH_{red}$ cluster models we have examined, a single important point emerges: where discrepancies between calculated and experimental geometries occur, such as in the orientation of the imidazole rings and carboxylate-type residues, or in the predicted protonation states of bridging ligands, the simple gas phase optimizations may have deficiencies, particularly for models containing only first-shell ligands. The quantum cluster models examined here clearly point toward the combined role that the protein and solvent environment plays in regulating the *soft modes* of the active site. This moderate or subtle "entatic" influence serves to lock the protein backbone and orient the various amino acid side chains, while, at the same time, where gaps in the protein network arise, ordered hydrogen-bonding networks between solvent and protein residues and between solvent molecules themselves are created that ensure that structural integrity is preserved. These subtle effects are largely associated with shallow potential energy surfaces, and further evidence bearing on such energetic issues in the protein environment will be presented in the following paper.[22b]

Note Added. The results of the calculations and structural observations within this manuscript are largely consistent with the findings of a new experimental paper, which we noted just prior to finalizing and submitting the present work, in which the structures of the oxidized, reduced, and mixed-valent form of MMOH from Mc have been crystallized and further examined in detail.[44]

Acknowledgment. This work was supported by NIH Grant GM43278 to L.N. We thank P. E. M. Siegbahn, D. A. Case, W.-G. Han, and J. M. Bollinger, Jr., for useful discussions and

(43) (a) Menage, S.; Brennan, B. A.; Juarez-Garcia, C.; Munck, E.; Que, L., Jr. *J. Am. Chem. Soc.* **1990**, *112*, 6423. (b) Kayatani, T.; Hayashi, Y.; Suzuki, M.; Uehara, A. *Bull. Chem. Soc. Jpn.* **1994**, *67*, 2980.

(44) Whittington, D. A.; Lippard, S. J. *J. Am. Chem. Soc.* **2001**, *123*, 827.

for providing preprints (J.M.B.) of manuscripts and unpublished data prior to publication. The reviewers are thanked for their pertinent commments prior to publication of this manuscript, D. McRee is acknowledged for use of the Xtalview progams, and we are especially grateful to E. J. Baerends and the Amsterdam group for use of the ADF codes.

Supporting Information Available: Figures for those active sites described in the text (but not shown) as well as a table of timing statistics for selected calculations. This material is available free of charge via the Internet at http://pubs.acs.org.

IC010115J